Combustion and Flame 251 (2023) 112679

Contents lists available at ScienceDirect

Combustion and Flame

journal homepage: www.elsevier.com/locate/combustflame

Neural network approach to response surface development for reaction model optimization and uncertainty minimization

Yue Zhang[a], Wendi Dong[a], Laurien A. Vandewalle[a,1], Rui Xu[a,2], Gregory P. Smith[b], Hai Wang[a,*]

[a] Department of Mechanical Engineering, Stanford University, Stanford, CA 94305 United States
[b] SRI International, Menlo Park, CA 94025 United States

ARTICLE INFO

Article history:
Received 21 December 2022
Revised 12 February 2023
Accepted 12 February 2023

Keywords:
Kinetic modeling
Neural network
Optimization
Uncertainty quantification
Uncertainty minimization

ABSTRACT

We examine the state-of-the-art neural network (NN) approach and its flexible implementations in combustion reaction model uncertainty quantification (UQ), optimization, and uncertainty minimization (UM). The work is motivated by addressing the problem of limited scalability of the traditional polynomial response surface methodology in handling large size of rate parameters and target data sets. Features of the NN training, accuracy, and trade-offs in several key aspects of the NN application are discussed. We show that for high-dimensional reaction model optimization and UM, a shallow NN with only one hidden layer is more robust and accurate than the polynomial response methodology. Further, we demonstrate that NN allows for adaptive training. New neural networks that augment new input parameters or updates in a trial reaction model can be adapted from the existing networks with much smaller training efforts. In addition, deep neural networks are capable of covering functional dependencies of initial thermodynamic conditions and boundary conditions, thus yielding generalized response surfaces with rate parameters and thermodynamic/mixture conditions as the input for a given combustion property. The NN approach can be readily integrated into the framework of the Method of Uncertainty Minimization using Polynomial Chaos Expansions (MUM-PCE) developed earlier. We present a test case that uses the trial Foundational Fuel Chemistry Model Version 2.0 (FFCM-2, a model consisting of 96 species and 1054 reactions for combustion of relevant C_{0-4} species), optimizing it against FFCM-1 targets, to illustrate the efficiency and accuracy of the NN method.

1. Introduction

Mathematical modeling of complex reacting systems is a multi-parameter problem. Many thermodynamic, chemical kinetic, and transport parameters have their inherent uncertainties [1]. Not only can these parameter uncertainties greatly impact the reliability of model predictions, but they also lead to added difficulties in uncovering missing reaction pathways [1–3]. Uncertainty quantification (UQ), and as importantly, uncertainty minimization (UM) is central to resolving these problems. The much-celebrated GRI Mech effort [4,5] represents an earlier approach to fundamental reaction model development and optimization. The approach uses the globally constrained error minimization and combines both the state of knowledge in reaction kinetic parameters (and their uncertainties) and modern diagnostics of species and measurements of global combustion properties to derive predictive reaction models. The need for uncertainty minimization (UM) was recognized later [2,6]. The UM approach reduces the model prediction uncertainty against a given set of experimental data, and it also enables us to explore internal consistency of a reaction model and external consistency of the model with available combustion data [2].

Critical to any kinetic model optimization and UM problems is the need of a surrogate model or response surface for each combustion experimental target [7]. Such a response surface premaps a predicted combustion property (e.g., ignition delay) with respect to the reaction model parameters, typically within their ranges of uncertainty, and in this manner, it resolves the numerical challenges during model optimization: rather than solving differential equations for each combustion response, the response values are evaluated simply using algebraic relationships. Several response surface methodologies have been used for reaction model

* Corresponding author.
E-mail address: haiwang@stanford.edu (H. Wang).
[1] Current address: ExxonMobil Technology and Engineering, Houston, TX 77380.
[2] Current address: Department of Chemistry and the PULSE Institute, Stanford University, Stanford, CA 94305; SLAC National Accelerator Laboratory, Menlo Park, CA 94025

https://doi.org/10.1016/j.combustflame.2023.112679
0010-2180/

optimization. Examples include sensitivity-based methods [8–10], High Dimensional Model Representation (HDMR) [11,12], and factorial based second-order polynomial representation [7]. Additionally, the Dakota code [13], developed for general computational engineering applications, employs response surface approaches ranging from polynomial to a stochastic layered perceptron network.

Earlier, we extended the use of second-order polynomial response to reaction model uncertainty minimization. The Method of Uncertainty Minimization using Polynomial Chaos Expansions (MUM-PCE) approach [2] optimizes the pre-exponential *A*-factors of Arrhenius rate parameters and reduces the model prediction uncertainty through the use of covariance matrix of the *A*-factors. Based on the Bayes' theorem, MUM-PCE assumes a log-normal distribution of rate parameters for the initial trial model and updates the posterior mean and covariance matrix given a set of combustion target data. It enables us to evaluate prediction uncertainties of a model analytically. Later, Tao et al. [14] extended this approach to co-optimizing the *A*-factors and activation energies. The MUM-PCE method has been demonstrated and used in a broad range of problems (see, e.g., [6,15–23]), and has been recently implemented in the `OpenSMOKE++` code (`OptiSMOKE++`) [24].

In an earlier effort, we used MUM-PCE to assimilate fundamental combustion data into the Foundational Fuel Chemistry Model Version 1.0 (FFCM-1) [25,26]. The resulting model has well-defined and reduced model uncertainties. FFCM-1 consists of 38 C_{0-2} species and 291 reactions, targeting the combustion properties of C_0-C_1 fuels. A set of 149 pre-selected, active rate parameters (including 99 pre-exponential factors and 50 third-body Chaperon efficiencies) were constrained against 146 experimental targets, from ignition delay time, laminar flame speed, to species time histories from shock tube and flow reactor experiments, covering a wide range of thermodynamic conditions. The choice of the active rate parameters was made through linear sensitivity analyses for each optimization target considered.

In a more recent effort, we extended FFCM-1 to C_{0-4} combustion chemistry. The effort was especially relevant to the recent HyChem modeling of real, multicomponent fuel combustion [27–33]. In particular, the accuracy of the HyChem reactions models was found to be particularly sensitive to the accuracy of the foundational C_{0-4} combustion chemistry [33]. The resulting FFCM Version 2.0 (FFCM-2) consists of 96 species and 1054 elementary reactions [34]. Compared to FFCM-1, FFCM-2 used a substantially larger target data set, consisting of 1192 independent combustion data targets. For such a high-dimensionality problem, the 2^{nd}-order polynomial response surface model was found to be severely limited in its scalability and accuracy. Not only is this traditional response surface approach computationally inefficient, the need for pre-selecting "active" rate parameters introduces significant biases and truncation errors in the response surfaces and thus the optimization result.

To resolve the problem just discussed, we note that the neural network (NN) approach is better suited for handling high dimensional input efficiently. Within the NN framework, deep neural network is a terminology coined for an artificial neural network that has two or more hidden layers as opposed to one-single hidden layer. NN has been applied to complex problems in many fields, from image classification [35], autonomous driving [36], gaming [37], to natural language processing [38]. A variety of transfer learning techniques [39] have been developed to enable efficient adaptation of existing NNs to new and similar tasks with great scalability. Likewise, neural networks have also been gaining popularity in combustion research [40–48]. For example, NNs have been shown to accelerate the computation of chemical terms in computational fluid mechanic solvers. Ji et al. [43] used Physics Informed Neural Networks (PINNs) with quasi-steady-state assumption (QSSA) to solve stiff chemical kinetic problems. Zhang et al. [44] designed a multi-scale sampling approach and developed a stable, three-hidden layer NN to predict the temporal evolution of chemical kinetics. NNs were shown to facilitate the discovery of reaction pathways from speciation time-history data. Ji et al. [45] proposed a chemical reaction neural network (CRNN) based on the law of mass action and Arrhenius law to interpret the neural network coefficients as reaction pathways and rate constants. NN has been used also in sensitivity analysis and optimization of combustion kinetic models [46]. Li et al. [47] developed NN-HDMR approach to calculate global sensitivity indices. They first constructed NN as a random sample generator and combined it with HDMR to improve the convergence and computational efficiency. Wang et al. [48] used the NN surrogate model with Markov chain Monte Carlo (MCMC) approach to optimize a methanol sub-reaction model.

In the present work, we examined the state-of-the-art NN approach and its implementation in MUM-PCE, targeting the UQ and UM problems of importance to combustion chemistry. Our NN implementation used the PyTorch library [49], which can be readily interfaced with Cantera [50]. The training, accuracy, and trade-offs in several key aspects of NN applications are discussed in detail. We show that for high-dimensional problems, such as FFCM-2, even a shallow NN with one hidden layer is more accurate than the polynomial response methodology, and as importantly both shallow and deep NNs are found to be substantially more scalable than the earlier polynomial method. The resulting NN response surfaces (NN-RSs) allows us to easily extract sensitivity coefficients. We demonstrate that NN-RS can be readily incorporated into the MUM-PCE framework. To evaluate NN-MUM-PCE, we present a test case that uses the trial FFCM-2 as the example, optimizing it against FFCM-1 targets (a subset of the FFCM-2 targets). Further, we demonstrate that NN can enable adaptive training. For example, new NN-RSs that augment new input parameters or updates in the trial rate parameters can be adapted from the existing NN-RSs with much smaller training sample sizes. Finally, NN-RSs can be extended to cover functional dependencies of initial thermodynamic conditions and boundary conditions, thus yielding broad response surfaces as functions of the rate parameters for an array of combustion responses.

2. Methodology

In this section, we discuss the mathematical frameworks for NN-RS, the extension of MUM-PCE to NN-MUM-PCE, the strategy for adaptive training, and the architecture of incorporating thermodynamic conditions into NN-RS.

2.1. Neural network problem setup

Neural network maps the *A*-factors of a reaction model into a combustion response y (e.g., laminar flame speed, ignition delay time, and species). As before [6,7], we first normalize the *A*-factors by

$$x_k = \frac{\log(A_k/A_{k,0})}{\log f_k}, \tag{1}$$

where A_k is the *A*-factor of the k^{th} rate parameter ($k = 1, \ldots, K_A$), $A_{k,0}$ and f_k are its nominal value (trial value) and uncertainty factor, respectively. In this way, x_k is bound as $x_k \in [-1, 1]$. The Chaperon efficiencies are normalized by

$$x_l = \frac{\log(\beta_{M,k}/\beta_{M,k,0})}{\log f_{M,k}}, \tag{2}$$

where $\beta_{M,k}$ is the M^{th} third body of the k^{th} reaction, and $\beta_{M,k,0}$ and $f_{M,k}$ are its nominal value and uncertainty factor, respectively.

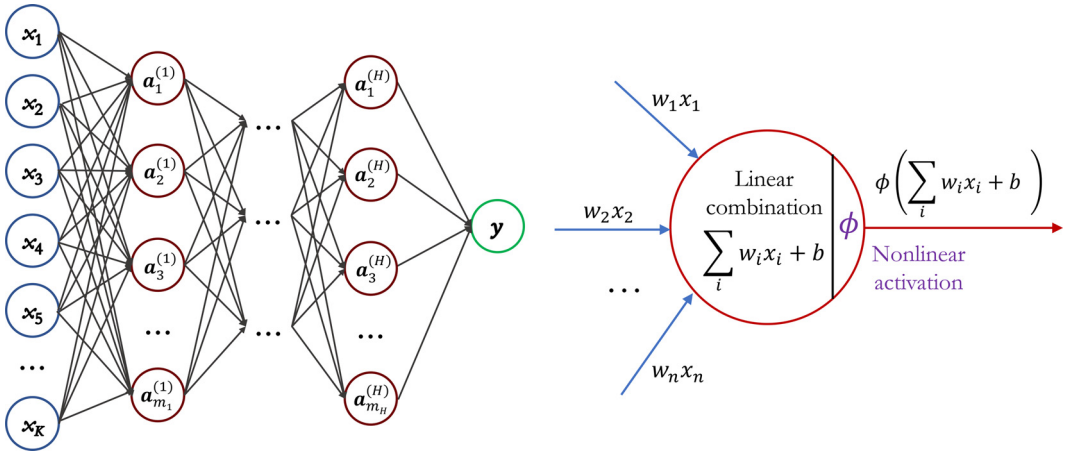

Fig. 1. A generalized neural network. Left panel: a schematic of the neural network architecture. The left most (blue) layer is the input layer of K input variables (normalized rate parameters); the right most (green) layer is the single-node output layer; the layers in between (red) are the hidden layers numbered as $1, 2, \ldots, H$, with $m_1, m_2, \ldots, m_H$ hidden nodes, respectively, for each layer. Right panel: a zoomed-in view of the mathematical operations in each hidden-layer node, including linear combination and nonlinear activation. (For interpretation of the references to colour in this figure legend, the reader is referred to the web version of this article.)

Here $l = K_A + 1, \ldots, K_A + K_M$, where K_M is number of Chaperon efficiencies considered in an optimization study.

Fig. 1 illustrates the general architecture of the neural network employed here. The first layer (input layer) is the $\mathbf{x}$ vector with dimension K, i.e., $\mathbf{x} = [x_1, \ldots, x_K]^T$. For example, in FFCM-2, we have $K_A = 1{,}029$ (excluding 25 chemiluminescence reactions from the 1054 reactions) and $K_M = 23$, so $K = K_A + K_M = 1{,}052$. The output layer is a scalar y, representing the response of a single combustion property. The layers in between are referred to as hidden layers. The number of hidden layers H and the dimensions for each hidden layer $m_1, m_2, \ldots, m_H$ are hyper-parameters to be determined during neural network training. As will be discussed later, we experimented with a wide variety of NN setups and found that a single hidden layer with 16 hidden nodes ($H = 1,\ m_1 = 16$) is appropriate for most combustion responses. Hence, unless it is otherwise indicated, our base-case NN setup uses $H = 1$, $m_1 = 16$.

A one-hidden layer NN-RS may be expressed by

$$y = \mathbf{W_2 a} + b_2, \mathbf{W_2} \in \mathbb{R}^{1\times m_1}, b_2 \in \mathbb{R}, \tag{3}$$

where

$$\mathbf{a} = \phi(\mathbf{z}) = ReLU(\mathbf{z}) = \max(0, \mathbf{z}), \tag{4}$$

and

$$\mathbf{z} = \mathbf{W_1 x} + \mathbf{b_1}, \mathbf{W_1} \in \mathbb{R}^{m_1\times K}, \mathbf{b_1} \in \mathbb{R}^{m_1\times 1}. \tag{5}$$

In the above equations, $\mathbf{W_1}, \mathbf{W_2}$, and $\mathbf{b_1}$ are vectors of coefficients and b_2 is a scalar, all to be trained. The function $\phi(\mathbf{z})$ introduces nonlinearity into the neural networks. For example, the Rectified Linear Unit (ReLU) [51] is a piece-wise linear function; it overcomes the vanishing gradient issue and gives rises to fast convergence to training than the traditional Sigmoid or Hyperbolic tangent functions [51]. Unless otherwise indicated, ReLU is used herein because of its simplicity. The resulting piece-wise linear function is sufficient as the higher-order dependencies to the rate parameters are insignificant for the combustion targets considered herein. The derivative of y is available analytically,

$$\frac{\partial y}{\partial \mathbf{x}} = \mathbf{W_1}^T \mathbf{W_2}^T \otimes \frac{\partial \phi(\mathbf{z})}{\partial \mathbf{z}}, \tag{6}$$

where

$$\frac{\partial \phi(\mathbf{z})}{\partial \mathbf{z}} = \left[d_j\right],\ d_j = \begin{cases} 1 & z_j > 0 \\ 0 & z_j \leqslant 0, \end{cases} \tag{7}$$

and $\otimes$ represents element-wise matrix multiplication. Equations (3), (4), (5) considers the rate parameters $\mathbf{x}$ as inputs only. In Section 2.5, we will discuss the possibility of incorporating thermodynamic conditions as inputs in addition to $\mathbf{x}$.

2.2. Sampling and data generation

Random sampling is unsuitable for high-dimensional problems, as it produces clusters and holes in the samples with reduced statistical efficiency. In the present work, we used Sobol sequence [52] instead. The Sobol sequence attempt to add sample points successively to positions as far away from existing sample points as possible so as to avoid clustering, and has been shown to converge rather efficiently [53]. The Sobol samples are inherently uniform with respect to the sampled space. Owing to the high dimensionality of the current problem, however, a uniform Sobol sample is inadequate because most samples would have been too far from the origin of the N-dimensional space [54], to an extent that the NN is especially under trained around the center of the parameter space. Since $\mathbf{x}$ is independently normally distributed with the bounds -1 and +1 being interpreted as the two-standard deviation for each rate parameter [2], the probability around $\mathbf{x} = \mathbf{0}$ is the highest with respect to model optimization and UM. For this reason, we designed a sampling approach that highlights the need of accuracy around $\mathbf{x} = \mathbf{0}$ and yet considers the far edge of the parametric space as well. Specifically, we carried out Sobol sampling following an inverse cumulative Gaussian distribution for a subspace given by the standard deviation of its samples. Three such subspaces were considered; Set 1 has a standard deviation of 0.1 in $\mathbf{x}$; Sets 2 and 3 have standard deviations of 0.3, and 0.5, respectively, as illustrated in Fig. S1 of the Supplementary Materials (SM). Set 3 has twice more sample points assigned to it than Sets 1 and 3. Together, the three sets form the complete sample set.

For FFCM-2 with 1052 parameters, we found a combined data sample size of 10,000 to be appropriate for the laminar flame speed and 40,000 to be appropriate for logarithms of the ignition delay and species concentration. The choice for the sample size takes into consideration the computational cost, effect sparsity, and the performance of the resulting NN-RS. The samples were partitioned as follows: 80% of data were randomly selected for NN training; 10% were used for validating the hyper-parameter choices; the remaining 10% were used for NN-RS validation.

Numerical simulations of the combustion properties were carried out using Cantera [50]. Laminar flame speed was calculated using over 400 mesh points covering an appropriate spatial domain, with multi-component transport and thermal diffusion. Igni-

tion delay time and species profile were simulated under adiabatic, and constant volume or constant pressure condition, depending on the nature of the shock tube experiment. For pressure-dependent unimolecular reactions, the *A*-factors of the high- and low-pressure limit rate coefficients were perturbed by the same factor to keep pressure fall-off in the rate coefficient unperturbed. Independent perturbation of the low-pressure limit rate coefficient and hence the fall-off is carried out through the perturbation of the selected Chaperon efficiencies for the same reaction. We used a modified, in-house Cantera code to allow perturbation of Chaperon efficiencies.

The performance of NN-RS depends heavily on the choice of the hyper-parameters [55]. Section S1 of the Supplementary Materials (SM) discusses the optimal approach to choosing the most important hyper-parameters.

2.3. Evaluation metrics and performance requirements

To evaluate the NN performance, we calculated the relative errors of the response values on the test data. We considered the mean error ($\varepsilon_{\text{mean}}$) and 95-percentile error ($\varepsilon_{95\%}$) as the key evaluation metrics, as listed in Table 1, because they are more indicative of the relevant parameter space away from sample outliers than the maximum error (ε_{max}). The requirements are most stringent near the center of the parameter space (i.e., Set 1 with $\sigma = 0.1$), and are more relaxed farther from the center (i.e., Set 2 with $\sigma = 0.3$ and Set 3 with $\sigma = 0.5$).

2.4. Adaptive learning and training

Adaptive training is another attractive NN feature over the conventional response surface methodology. Notably, a response surface trained for a combustion property does not lend any information to the training of a new surface of a related combustion property (e.g., ignition delay times of identical mixture conditions, but with slightly different temperature or pressure). More importantly, the trial reaction model often requires several updates during a typical optimization and uncertainty minimization process. And each time such an update occurs, the entire set of response surfaces must be regenerated without being able to leverage the information available from a previous generation of the response surfaces.

In NN, transfer learning or adaptive training refers to an approach in which we re-purpose a model trained on an old task and use it on a new task. If the two tasks share similar structures and patterns, the neural network leverages what it has already learned and adapts to the new task with a few number of training samples and a shortened training time. An obvious application of transfer learning is to use an NN already trained for a thermodynamic condition to the training of a new NN under related thermodynamic conditions. Fig. 2 presents two other examples of adaptive training. The first case adds or splits one or more rate parameters to the trial model (for example, adding a missing reaction, or splitting out the Chaperon efficiency of a pressure dependent reaction and treating it an independent variable). In the left panel of Fig. 2, we initialize all coefficients of the new NN with the old coefficients except for the parameter(s) that is/are added or split. The right panel of Fig. 2 illustrates the update of two rate parameters (x_1 and x_5) in the trial model (e.g., changes in activation energy or temperature exponent in the modified Arrhenius equation). Here, the modified parameters are randomly initialize while all other coefficients are taken fron a prior NN. These initialization strategies enable the NN to adapt to new tasks with a substantially smaller sample size.

Adaptive training is sensitive to the choice of learning rates. In general, a small learning rate is necessary such that the training processes does not entirely unlearn from the previous training. Examples will be given in Section 3.2, illustrating the utility of adaptive learning.

2.5. Extending NN-RS with thermodynamic conditions as input

In the polynomial response surface method used earlier [4,15], the rigidity of the polynomial functional form renders it impossible to consider thermodynamic conditions or boundary conditions as possible inputs in a response surface, and each optimization target would require a separate response surface. Here we show that NN is capable of incorporating the thermodynamic conditions as inputs in addition to rate parameters **x**. Fig. 3 presents a schematic illustrating the NN architecture. Inherently, such an NN must necessarily be deep NN with more than one hidden layer. In the input layer, **x** and a set of thermodynamic conditions (e.g., temperature T, pressure p, mixture composition **X**) are processed with two separate sets of NN parameters. The two vectors in the first hidden layer have the same dimension. They are concatenated before feeding into the next hidden layer to make predictions. The two-tower architecture makes it easier and more efficient for the extended NN-RS to learn the dependency on the thermodynamic conditions. The first hidden layer for rate parameters reduces the dimensionality of **x**; the second hidden layer enables the thermodynamic conditions processed to interact with key kinetic parameters only. In contrast, directly appending the thermodynamic conditions into an NN effectively treats T, p and **X** simply as some new variables, leading to a higher dimensional input that makes learning less efficient.

The extended NN architecture is best utilized with physical considerations or insights. For example, for ignition delay, constraining the forms of input for T and **X** following the Lifshitz empirical function [56] not only improves the NN-RS performances within the range of thermodynamic conditions considered, it also allows for extrapolation to conditions outside of the initial range considered. This physics-guided NN feature will be specifically presented and discussed in Section 3.3.

2.6. Implementing neural network in MUM-PCE and for other related applications

It is evident that the NN-RS can be used for extracting the gradient $\partial y/\partial x_k$ and hence, the global and local sensitivity coefficients, as discussed in Section S3 of the SM. Here we focus our discussion on the implementation of NN-RS into MUM-PCE. Details of MUM-PCE can be found elsewhere [2], Briefly, MUM-PCE allows for constraining a reaction model to better predict a set of combustion property targets, and as importantly, reduces model prediction uncertainty via the rate-parameter covariance matrix. We define the objective function as

$$\Phi(\mathbf{x}^*) = \min_{\mathbf{x}} \left\{ \sum_{m=1}^{M} \left(\frac{y_m(\mathbf{x}) - y_{m,obs}}{\sigma_{m,obs}} \right)^2 + \lambda ||\mathbf{x}||_2^2 \right\}, \tag{8}$$

where M is the number of experimental targets. The first term of Eq. (8) is the cost function; it measures the deviation between the model prediction $y_m(\mathbf{x})$ and the experimental value $y_{m,obs}$. The second term is the Euclidean norm of the normalized rate parameter **x**, measuring the distances of the optimized rate parameters from the trial assignments. Each target m is inversely weighted by the its experimental uncertainty $\sigma_{m,obs}$. In the second term, λ is a regularization coefficient, governing the weight applied to the reaction kinetics relative to combustion property data. For example, in FFCM-1, $\lambda = 4$.

In the FFCM-1 effort, MUM-PCE implements the Levenberg-Marquardt (LM) algorithm [57] to solve the nonlinear least-square

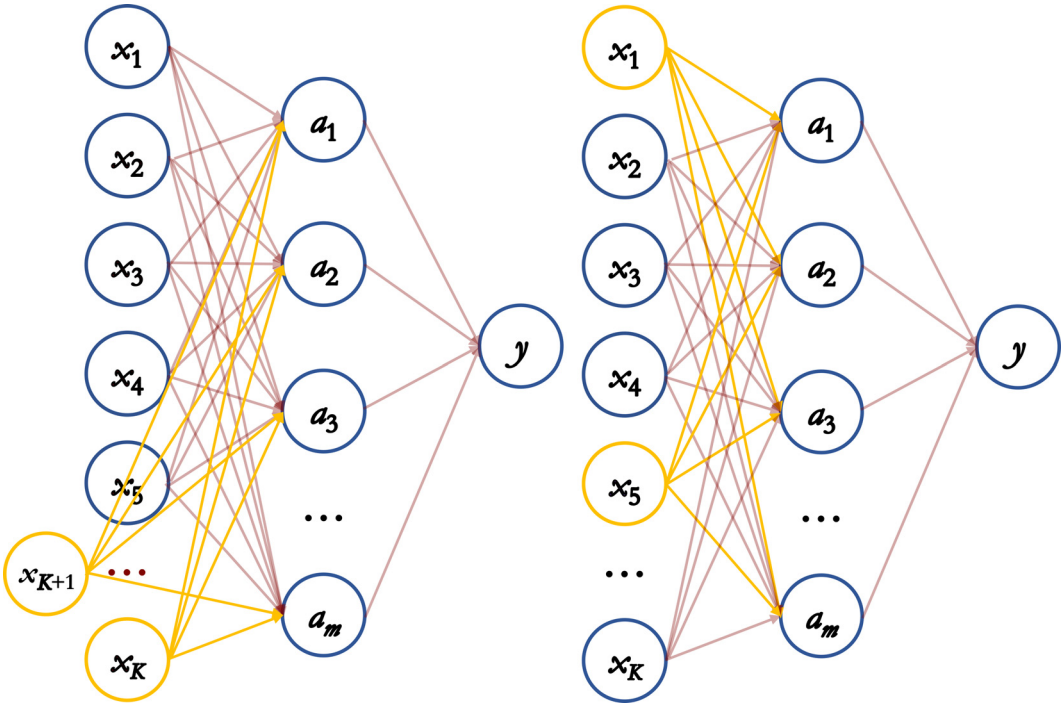

Fig. 2. Adaptive training of NN-RS using transfer learning. Left panel: adapting to input parameters due to an added reaction (x_{K+1}) or with a parameter splitting (x_K) splitting into two parameters (x_K and x_{K+1}); Right panel: adapting to changes in Arrhenius expressions (highlighted as x_1 and x_5). In both case, the parameters in yellow circles are initialized randomly to account for changes in the kinetics, while all other parameters in blue circles may be initialized using values from a previous NN-RS. (For interpretation of the references to colour in this figure legend, the reader is referred to the web version of this article.)

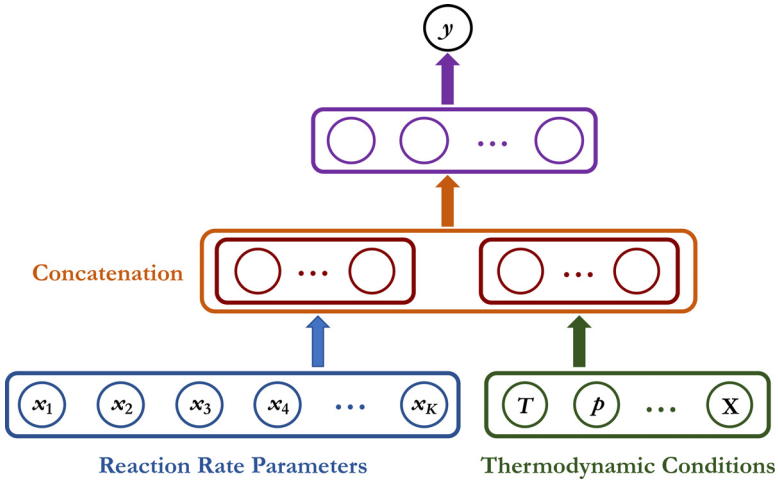

Fig. 3. A generalized NN-RS architecture that incorporates the thermodynamic conditions as input. For the bottom layer, the normalized reaction rate parameters **x** (in blue) and thermodynamic conditions (eg., temperature T, pressure p and mixture composition **X**) (in green) are processed as two separate sets of coefficients. In the second layer, the two processed vectors (red) are concatenated (orange) and passed through the third layer (purple) to predict the combustion responses. (For interpretation of the references to colour in this figure legend, the reader is referred to the web version of this article.)

problem. LM works well for low-dimensional, unbounded problems. FFCM-2, however, is an exceptionally higher-dimensional, sparse problem. We applied the trust region reflective (TRF) algorithm from the SciPy nonlinear least squares optimizer [58]. TRF explicitly applies the parameter bounds so that the optimized rate parameters are more interpretable. The TRF algorithm also requires as input the gradient of y, which is available analytically, as discussed before.

The posterior covariance matrix may be obtained by linearizing the response surface after optimization [2]. Assuming the rate parameters distribute as a multivariate log-normal distribution, we represent the optimized rate parameters $\mathbf{x}^*$ as

$$\mathbf{x}^* = \mathbf{x}^{(\mathbf{0})*} + \mathbf{x}^{(\mathbf{1})*}\xi, \tag{9}$$

where $\xi \sim \mathcal{N}(0,1)$ is a standard normal random variable; the mean $\mathbf{x}^{(0)*}$ is the optimized rate parameters. By applying the Bayes' theorem with Gaussian prior, the covariance matrix Σ^* is:

$$\Sigma^* = \mathbf{x}^{(\mathbf{1})*}\mathbf{x}^{(\mathbf{1})*T} = \left(\sum_{m=1}^{M} \frac{\mathbf{J_m}^T\mathbf{J_m}}{\sigma^2_{m,obs}} + \lambda\mathbf{I}\right)^{-1}, \tag{10}$$

where $\mathbf{I}$ is the identity matrix, and $\mathbf{J_m}$ is the Jacobian matrix evaluated at the optimal point

$$\mathbf{J_m} = \frac{\partial y}{\partial \mathbf{x}}|_{\mathbf{x}=\mathbf{x}^{(\mathbf{0})*}}. \tag{11}$$

The prediction uncertainty of the trial or optimized model σ^*_m can then be calculated using polynomial chaos expansions,

$$\sigma^*_m = ||\mathbf{J_m}^T\mathbf{L}||^2_2 + \lambda||\mathbf{L}^T\mathbf{H_m}\mathbf{L}||^2_F, \tag{12}$$

where $\mathbf{J_m}$ and $\mathbf{H_m}$ are the Jacobian and Hessian matrix at the optimal point, and $\mathbf{L}$ is the Cholesky decomposition of the covariance matrix. For the trial model, the covariance matrix is a diagonal matrix given by $\frac{1}{\lambda}\mathbf{I}$. For the optimized model, the covariance matrix is given by Eq. (10). For NN-RS with ReLU activation, the second term vanishes because Hessian matrix is zero.

MUM-PCE evaluates the consistency of reaction model with respect to the experimental data by calculating the F score of a target m as

$$F_m = \frac{y_{m,obs} - y_{m,opt}}{2\sigma_m}, \tag{13}$$

where $y_{m,opt}$ is the optimized model prediction. A target m is regarded as inconsistent when $|F_m| > 1$. That is, the optimized model cannot reconcile the target within its experimental uncertainty by adjusting the rate parameters within the uncertainty limits. The inconsistent targets are removed from the target list and the model is re-optimized. This process is carried out iteratively until all remaining targets are consistent. The inconsistent targets are usually further examined to understand the source of inconsistency.

We discuss the workflow of NN-MUM-PCE framework in Section S4 of the Supplementary Material (SM), and highlight several key features here. Unlike the original MUM-PCE [2], in which active parameters are pre-selected from a linear sensitivity analysis for each target and the remaining (inactive) parameters are frozen, the current NN-RS, in principle, allows for all rate parameters to be perturbed and optimized. While the benefits of this new capability will be illustrated later, freezing unnecessary parameters is useful to suppressing noises and produces optimization results that are easier to interpret. In NN-MUM-PCE, a parameter x_k does not contribute to improving model prediction or reducing the prediction uncertainty if $|A_k/A_{k,0} - 1| < \chi_x$, and when the optimized uncertainty of x_k is larger than χ_σ, where χ_x is the multiplier threshold, and χ_σ is the uncertainty threshold. Such a parameter is frozen (not optimized). Hence, two sets of rate parameters result from this procedure, the optimized set $\mathbf{x_a}$ and the unoptimized set $\mathbf{x_f}$. We then apply the conditional normal distribution to obtain the mean and covariance matrix for $\mathbf{x_a}$ analytically as

$$\mathbf{x} \sim \mathcal{N}(\mu, \mathbf{\Sigma}) = \mathcal{N}\left(\begin{bmatrix}\mu_\mathbf{a}\\ \mu_\mathbf{f}\end{bmatrix}, \begin{bmatrix}\mathbf{\Sigma_{aa}} & \mathbf{\Sigma_{af}}\\ \mathbf{\Sigma_{fa}} & \mathbf{\Sigma_{ff}}\end{bmatrix}\right), \tag{14}$$

where

$$\mu_\mathbf{a}|_{\mathbf{x_f}=\mu_f} = \mu_\mathbf{a} + \mathbf{\Sigma_{aa}}\mathbf{\Sigma_{ff}^{-1}}(\mathbf{x_f} - \mu_\mathbf{f}), \tag{15}$$

$$\mathbf{\Sigma_a}|_{\mathbf{x_f}=\mu_\mathbf{f}} = \mathbf{\Sigma_{aa}} - \mathbf{\Sigma_{af}}\mathbf{\Sigma_{ff}^{-1}}\mathbf{\Sigma_{fa}}. \tag{16}$$

Suffice it to note that NN-MUM-PCE allows for sequential optimization of combustion reaction models. In this case, all kinetic parameters remain active in the NN response surfaces, and which subset of the parameters are to be optimized is specified in the optimization stages. Because of the hierarchical nature of combustion chemistry, the prediction uncertainty of a reaction model for the combustion of a larger hydrocarbon fuel relies on an uncertainty-minimized model of smaller hydrocarbons. In principle, the sequential optimization strategy allows us to exploit such structures and extend our studies to new fuels readily.

3. Results and discussion

3.1. Comparison of polynomial response to neural network response

To demonstrate a key advantage of the NN approach, we first discuss the truncation errors in conventional 2^{nd}-order polynomial response surfaces. As discussed earlier, 2^{nd}-order polynomial response surfaces based on a fractional factorial design has a limited scalability. The minimal number of training samples required is $(n^2 + 3n)/2 + 1$, where n is the number of "active" rate parameters selected from a sensitivity analysis. Many of the past studies assumed $n = 20$ [2,4–6]. Fig. 4 shows the truncation errors of three $n = 20$, 2^{nd}-order polynomial response surfaces, one each selected for the laminar flame speed S_u^0 (a stoichiometric C_2H_2/air mixture at 300 K unburned gas temperature and 1 atm pressure), and the ignition delay τ_{ign} and peak CO mole fraction X_{CO} (1.32% C_2H_4-3.95% O_2-94.73% Ar, $T_5 = 1300$ K, $p_5 = 15$ bar). We tested these polynomial response surface on two test data sets: one that only varies the 20 active parameters (the top row), the other that allows all 1052 parameters of FFCM-2 to vary (the bottom row). As observed, the polynomial responses are sufficiently accurate within the active parameter spaces, but they are grossly inaccurate when the initially assumed "inactive" parameters are varied due to truncation error.

As expected, increasing the number of "active" parameters improves the performance of the 2^{nd}-order polynomials. Fig. 5 shows the maximum relative error, 95-percentile relative error, and mean relative error for the polynomial responses (symbols) built using 40,000 sample points, as a function of the number of active parameters n considered. In each case, we again used 2000 sample points for testing, and all parameters were allowed to vary. The initial drop of the relative errors from $n = 20$ to $n \approx 70$ to 80 is caused by the reduction of the truncation errors, and the results shown in Fig. 5 suggest that a full consideration of the active parameters in response surface development requires from 60 to 80 active parameters, depending on the type of the combustion responses. The relative errors exhibit a U-shaped dependence on n. For large n values, the errors increase due to bias-variance tradeoff for polynomial fittings [54].

Another aspect of the problem is the number of samples needed for polynomial and NN-RS training. Fig. 6 compares the performance of a $n = 70$, 2^{nd}-order polynomial and NN-RS in terms of the relative errors as we increase the number of the samples used for training. To evaluate the performance, we used an identical set of 2000 samples to test all surfaces generated. Furthermore, to understand the convergence of the polynomial and NN-RS performance with respect to the training sample size, we repeated the training 10 times at each sample size; and each set of sample is extracted from a full set of Sobol sample of 40,000 points. This procedure allows us to derive the mean and standard deviation of the relative errors of each type of the response surfaces with respect to the training sample size. Fig. 6 shows the performance evolution of the polynomial and NN-RS. Here, we used the ignition delay time of a stoichiometric CH_4/O_2 mixtures diluted in 77.5% CO_2 ($T_5 = 1374$ K, $p_5 = 27.1$ atm) as the example. Several features can be observed from Fig. 6. For sample sizes $\leqslant 3000$, the trained surfaces generally have relative errors with large standard deviations, thus indicating the lack of convergence at those sizes for both type of the surfaces. This is especially true for the NN-RS; when trained on only 3000 samples, both the errors and its spread are rather large. The errors in the 2^{nd}-order polynomial decay faster with respect to the sample size. This fast decay rate is certainly associated with its substantially smaller dimension of the parameter space ($n = 70$) than that of the NN-RS with $n = 1{,}052$. Also because of the difference in the dimensionality, the polynomial is converged with around 15,000 training points, while the NN-RS requires more training points to achieve the same accuracy. Importantly, the training of this 1052 dimensional NN-RS requires only three to four times more samples than that of the polynomial of 70 dimensions.

The impact of the NN architecture is evaluated next. As shown in Fig. 1, two key parameters define the complexity of an NN. They are the number of hidden layers H and the number of the nodes within each hidden layer m_h ($h = 1, \ldots, H$). Fig. 7 shows the variations of $\varepsilon_{\text{mean}}$ and $\varepsilon_{95\%}$ of the NN-RSs as a function of m_1 for a

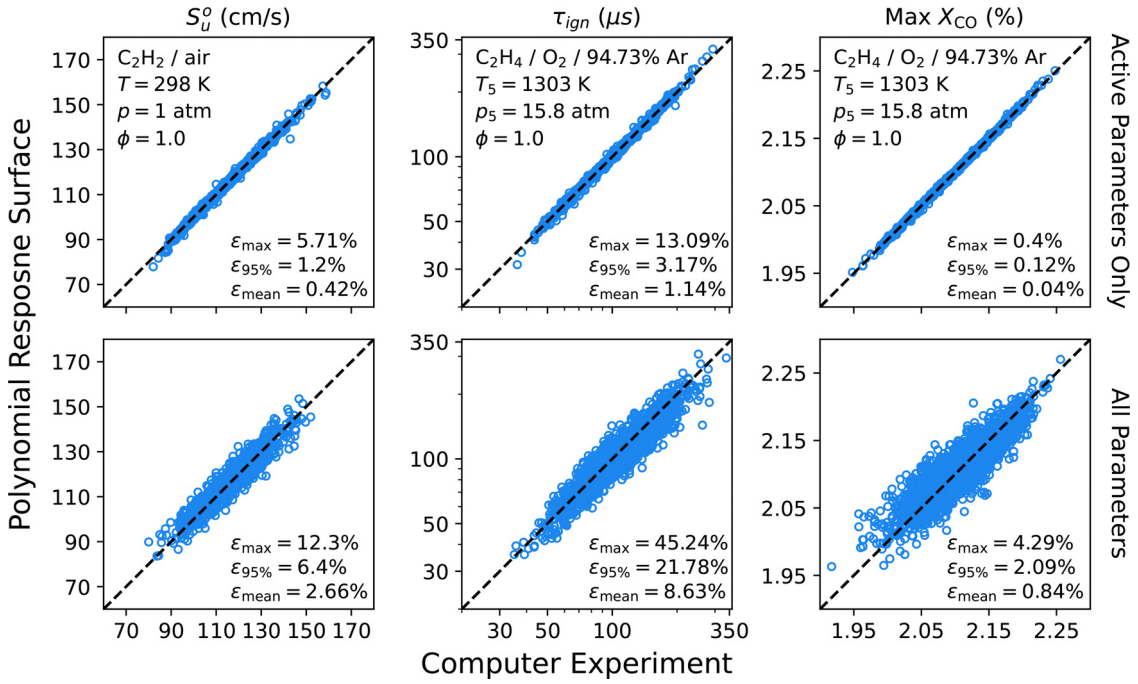

Fig. 4. Truncation errors of $n = 20$, 2^{nd}-order polynomial response surfaces for three types of sample combustion responses. For each case, the polynomials were trained on 20,000 (Sobol) sample points, and the test data consist of 2000 samples. Top row: testing on data that vary the "active" parameters only; bottom row: testing on data that vary all 1052 parameters; Left column: laminar flame speed (S_u^o); middle column: ignition delay time (τ_{ign}); right column: peak CO mole fraction (X_{CO}).

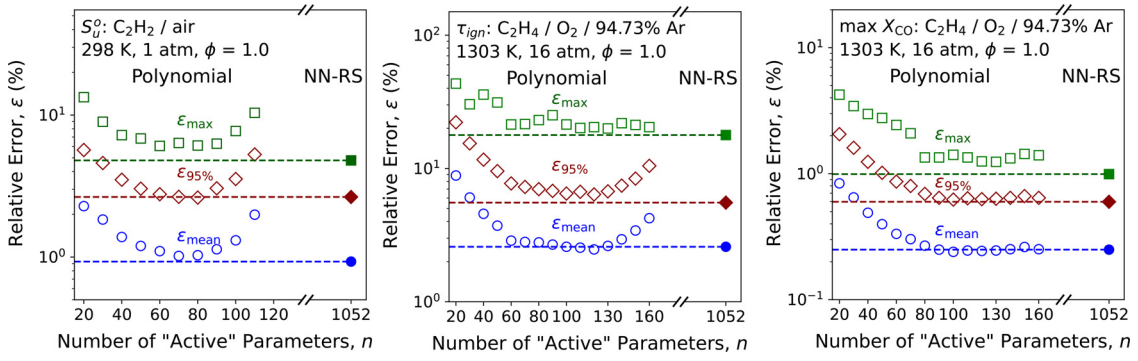

Fig. 5. Relative errors of the 2^{nd}-order polynomial (open symbols) and neural network (closed symbol) response surfaces for three sample types of combustion response. The "active" parameters in the 2^{nd}-order polynomials are selected based on the ranked local sensitivity ($n < K$) for each case, and the NN-RSs allow all parameters to vary (i.e., $n = K = 1{,}052$). The dashed lines are drawn to guide the eyes and for comparison with the polynomials. Left: laminar flame speed; middle: ignition delay time; right panel: maximum CO mole fraction, under conditions shown in each respective panel.

Table 1
NN-RS performance requirements: mean relative errors ε_{mean} and maximum 95-percentile relative errors $\varepsilon_{95\%}$ allowed for each sub-test sets.

Test set	Mean error (ε_{mean})	95-percentile error ($\varepsilon_{95\%}$)
1 ($\sigma = 0.1$)	1%	2%
2 ($\sigma = 0.3$)	2%	5%
3 ($\sigma = 0.5$)	3%	10%

single hidden later ($H = 1$) (left panel) and as a function of H for a fixed $m_h = 16$ for $h = 1, \ldots, H$ (right panel). The example shown is again the ignition delay time of a stoichiometric CH_4/O_2 mixture diluted in 77.5% of CO_2 at $T_5 = 1374$ K and $p_5 = 27.1$ atm. Here, all $n = 1052$ rate parameters were considered, and the training sample set is held the same, with 60,000 training points. The tests shown in Fig. 7 were made with Test set 2 (Table 1) with 2000 points. It is seen that as we increase the number of nodes in a single hidden-layer NN, the errors first decrease until $m_1 \approx 50$ and then it increases for $50 < m_1 < 64$. For $m_1 > 64$, the performance of the NN-RS improved again as m_1 increases. This complex, double-descent behavior has been discussed in [59]. Briefly, the worst choice for an NN is when $K \times m_1$ is approximately equal to the training sample size. More accurate NNs are typically those that are either under-parameterized or over-parameterized. Although an NN with 32 nodes gives more accurate results, the larger number of nodes translates into great computational demand. For this reason and considering the accuracy requirements listed in Table 1, we opt for 16 nodes in our base-case NN. The right panel of Fig. 7 shows the relative errors of four NNs, varying the number of hidden layers from $H = 1$ to $H = 4$, while keeping the number of nodes at 16 for each hidden layer. Clearly, the impact of H on the performance of the NN-RS is, by all means, mild. It is for this reason that we employ a single hidden-layer NN as our base case study.

Note that the analysis also provides key insight about the number of training sample points for NN development. For polynomial responses, the minimum number of training samples required can

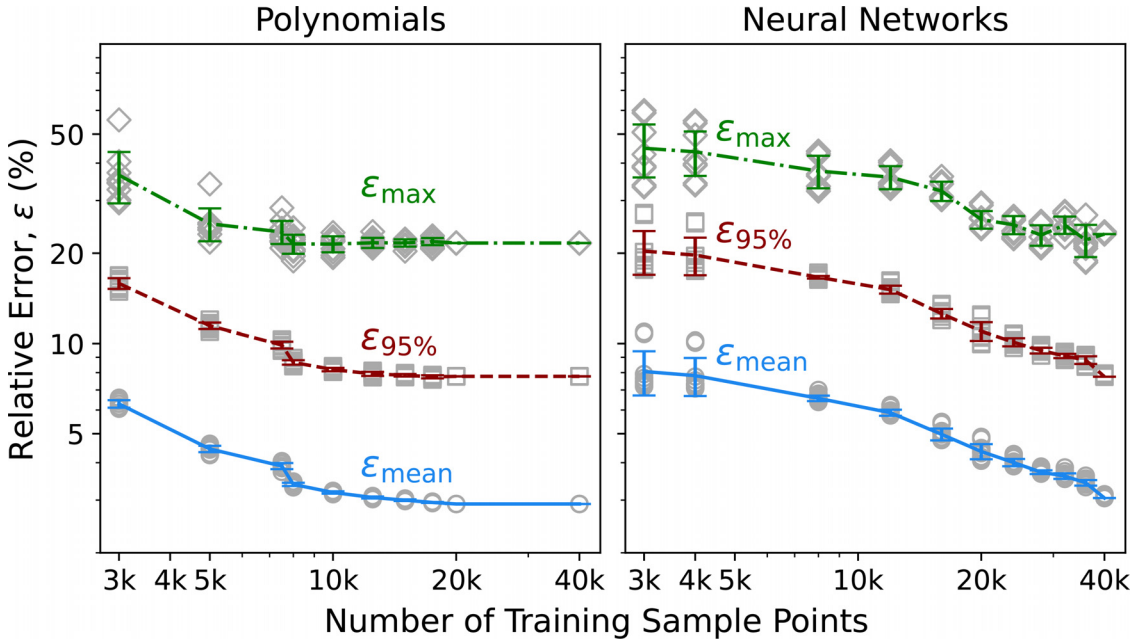

Fig. 6. Variations of the relative errors, comparing 2^{nd}-order polynomial with $n = 70$ and NN-RSs with $n = 1052$, as a function of the sizes of the training set, using ignition delay time of a stoichiometric CH_4/O_2 mixtures diluted in 77.5% CO_2 ($T_5 = 1374$ K, $p_5 = 27.1$ atm) as the example. The test sample size is 2,000. Symbols represent the errors evaluated for the response surfaces trained on several randomly selected training samples, and lines and error bars are the mean error and its standard deviation at each training sample size.

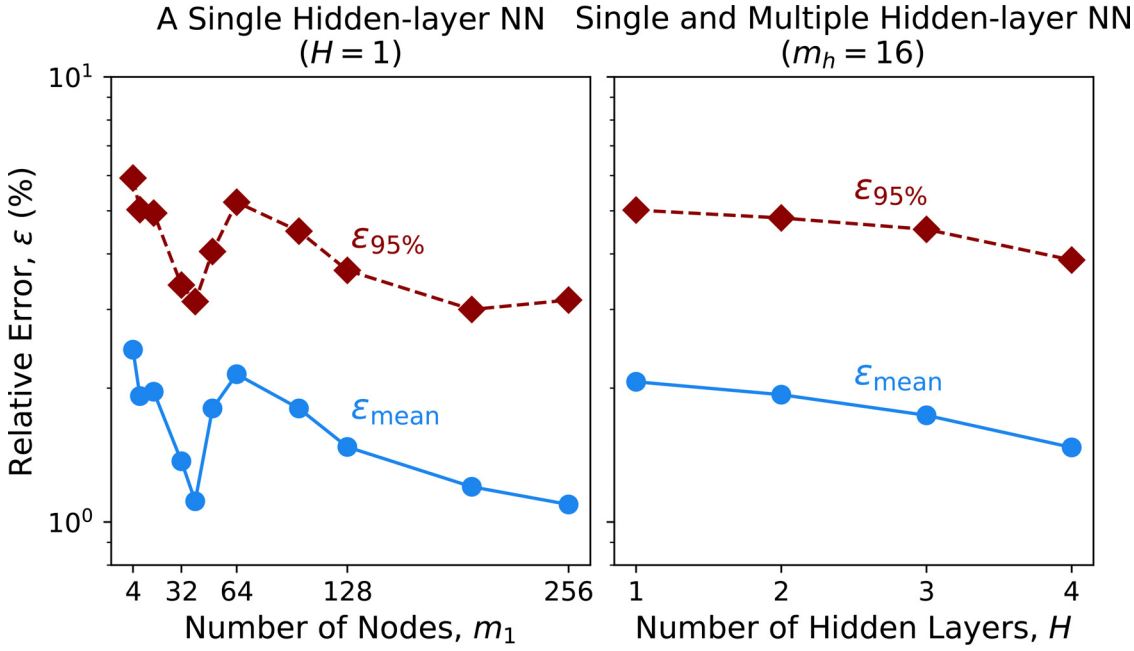

Fig. 7. Variations of the relative errors of a single hidden-layer NN (left) as a function of the number of nodes m_1 and of single-versus-multi-hidden layer NNs (right), all with 16 nodes, as a function of the number of hidden layers, H, using ignition delay time of a stoichiometric CH_4/O_2 mixtures diluted in 77.5% CO_2 ($T_5 = 1374$ K, $p_5 = 27.1$ atm) as the example. The training sample size is 60,000; tests use Set 2 (Table 1) with 2000 sample points.

be calculated, as discussed before. For NNs, there is not a deterministic approach yet, because the performance of NNs depend on many more factors. Yet, one of the key factors is the initialization of NN parameters. We will show in Section 3.2 that a good initialization can significantly reduce the number of training samples needed.

To briefly summarize, the advantage of NN is that even though its training may require a larger training sample set, a single hidden-layer, 16-node NN-RS is particularly attractive to handling large models; and without having to pre-select active parameters, this NN approach is highly scalable for response surface generation.

3.2. Adaptive NN training

The increased computational demand for NN training may be alleviated by adaptive training, which uses the NN parameters of an trained NN as the initial input to the training of a new NN for a related set of input parameters or thermodynamic conditions. The reason why adaptive training increases the training efficiency of

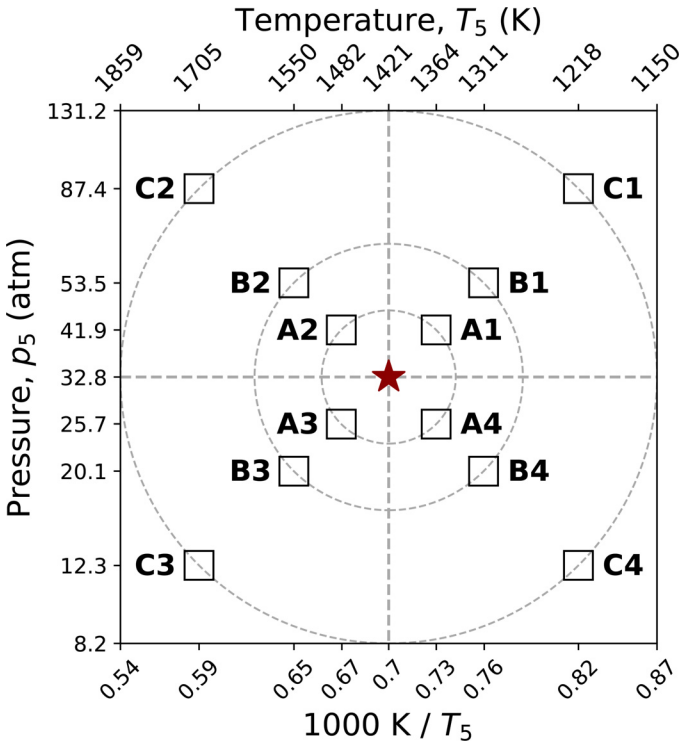

Fig. 8. Selected thermodynamic conditions for adaptive training using the NN already trained for the ignition delay of a stoichiometric $CH_4/O_2/77.5\%$ CO_2 mixture at the nominal p_5 and T_5 condition marked by the center star. Three sets of new conditions are tested with each set containing the variations of both p_5 and T_5. The set closest to the nominal condition is denoted as set A*i*; the intermediate set is B*i*; the furthest set is C*i* ($i = 1, \ldots 4$), which extends p_5 from 12.3 atm to 87.4 atm, and of T_5 from 1,218 K to 1,705 K.

new NN is clear. The NN parameters implicitly contains the sensitivity information. As long as the sensitivity is similar, the already trained NN contains "prior" knowledge that must be useful to training related NNs.

Here, we demonstrate adaptive training on several examples. In the first example, we use the ignition delay time of a stoichiometric CH_4-O_2-77.5% CO_2 mixture, and define the center star of Fig. 8 as the nominal p_5 (32.8 atm) and T_5 (1421 K) condition. We examine adaptive training efficiencies of the neighboring points over the ranges of p_5 from 12.3 atm to 87.4 atm, and of T_5 from 1,218 K to 1,705 K, also shown in Fig. 8. Fig. 9 shows the rates of convergence of the NNs for each condition, comparing adaptive training using the NN parameters obtained at the nominal condition and direct training without using the prior knowledge. For all condition sets, the adaptive training (solid lines) always yield faster convergence than without adaptive (dashed lines). If we examine the tolerable mean and 95-percentile errors corresponding to the Set 2 test data (see, Table 1 and the horizontal dash-dotted-dash lines of Fig. 9), the NNs of the closest neighbors of the nominal condition (Set A) are sufficiently accurate when adaptively trained on only 400 samples. Without adaptive training, the NNs require about 10,000 training samples to achieve the same accuracy. As expected, the efficiency of adaptive training decreases for set C with p_5 and T_5 values being furthest from the nominal condition. Even so, adaptive training is always preferable, as it can be seen in the bottom row of Fig. 9.

Next, we consider two examples in which new rate parameters are adapted into the base-case NN. The first test case is the ignition delay time of a stoichiometric C_2H_6/O_2 mixture diluted in 91% argon with $T_5 = 1434$ K and $p_5 = 7.56$ atm. The base NN does not consider the Chaperon efficiency of Ar in the reaction C_2H_4 + H (+M) $\rightleftharpoons$ C_2H_5 (+M) separately form those of other third bodies.

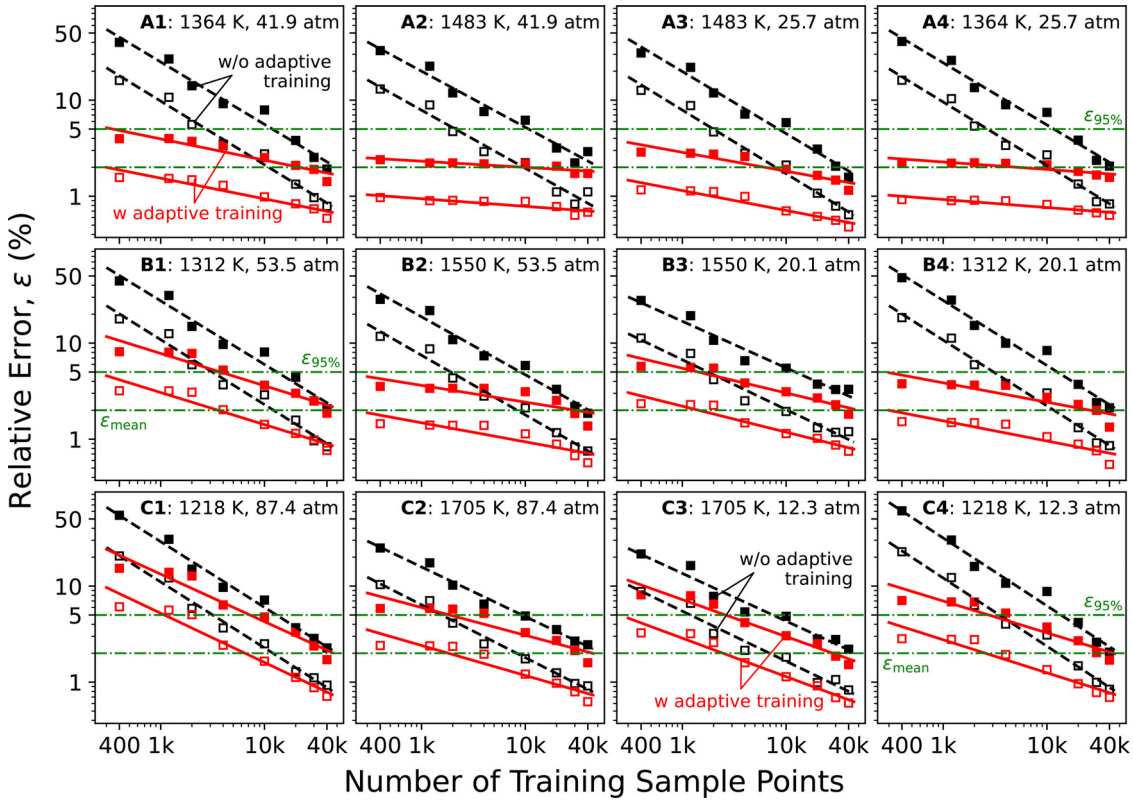

Fig. 9. Comparison of mean (open symbols) and 95-percentile (filled symbols) errors as a function of the number of samples used for NN training, comparing adaptive training (solid lines) and without adaptive training (dashed lines) for the three sets of conditions (A*i*: top panels, B*i*: middle panels, and C*i*: bottom panels, for $i = 1, \ldots 4$) shown in Fig. 8. The horizontal dashed-dotted-dashed lines indicate the mean and 90-percentile error tolerance levels. Tests use Set 2 of Table 1 with 2000 sample points. Lines are drawn to guide the eyes.

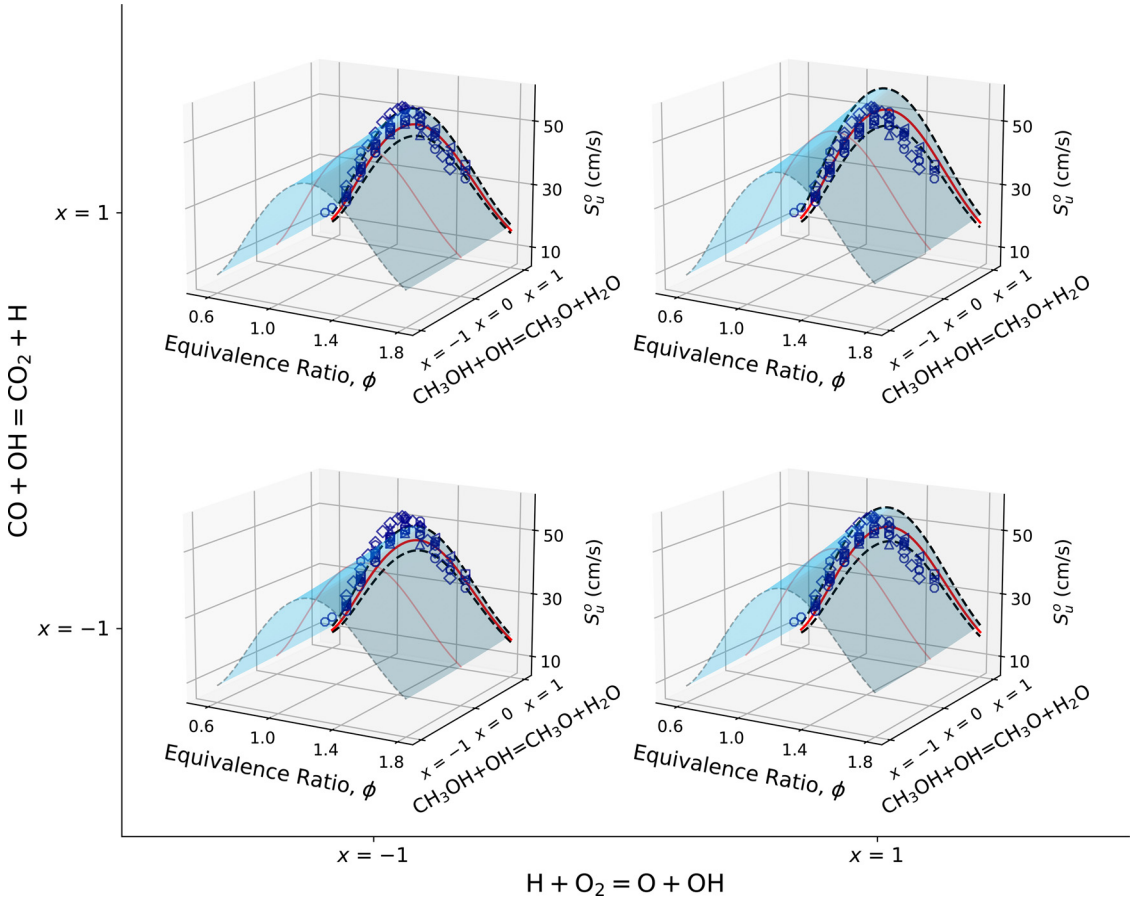

Fig. 10. Projections of a generalized NN-RS of the laminar flame speed of CH_3OH/air mixtures ($T_0 = 298$ K, $p = 1$ atm and $0.6 \le \phi \le 1.8$). The NN-RS, given as $y_{S_u^\circ}(\mathbf{x}, T_0, p, \phi)$, covers the ranges of thermodynmaic conditions of 298 K $\le T_0 \le$ 450 K, $0.5 \le p \le 10$ bar, and $0.6 \le \phi \le 1.8$, and rate parameters $\mathbf{x} = [x_1, \ldots, x_K]^T$, where $K = 1052$) On the $S_u^\circ - \phi$ planes, symbols are experimental data under the same $T_0 = 298$ K and $p = 1$ atm condition: ◇ Bardin et al. [62]; □ Davis and Law [63]; ○ Egolfopoulos et al. [64]; ◁ Guelder [65]; ▷ Katoch et al. [66]; ▽ Metghalchi and Keck [67]; △ Sileghem et al. [68]; ⬡ Saeed and Stone [69]; ◯ Vancoillie et al. [70]; ☆ Voss et al. [71]. The outer axes show limiting rate values for reactions $H + O_2 \rightleftharpoons O + OH$ and $CO + OH \rightleftharpoons CO_2 + H$. In each panel, NN-RS predictions are projected to the $S_u^\circ - \phi$ planes to illustrate the nominal model prediction (solid line) and model uncertainty (dashed lines) caused by the rate uncertainty of $CH_3OH + OH \rightleftharpoons CH_3O + H_2O$ under each condition.

Suppose that later it is realized that the Chaperon efficiencies of Ar, N_2 and H_2O must be treated separately in optimization against the ignition delay (in argon) and laminar flame speed (in N_2, where M = H_2O exerts a notable impact on the flame speed). Splitting M into M = Ar, M = H_2O and M = Ar and all other species forms an extended NN, which needed only 4000 samples or 10% of those in the base case for its training. Table S1 of the SM provides comparisons of the ranked first-order sensitivity coefficients calculated by the brute force method with those evaluated from the NN-RS adaptively trained and the NN-RS without adaptive training. The results are nearly identical. In the second case, we consider reaction model updates focusing on the *iso*-butene sub-model. A total of 13 *iso*-butene related reactions were updated from the original FFCM-2 trial model, including the H-abstraction by O_2 of *i*-C_4H_8 by considering recent theoretical calculation [60] and low-temperature rate measurements [61]. We used the ignition delay time of 2% *iso*-butene (*i*-C_4H_8)-12% O_2 diluted in Ar at $T_5 = 1556$ K and $p_5 = 1.7$ atm as the test case. Adaptive NN training required 12,000 training samples (about 30% of the original training data) to achieve the same accuracy of the base case NN. The ranked sensitivity coefficients differ significantly before and after the rate updates, as it can be seen in Table S2, because of the updates led to reaction pathway changes during *i*-C_4H_8 oxidation. Yet, the significantly reduced number of training samples indicate useful knowledge transfer from the base-case NN to the adapted NN, which comes from key reactions beyond the *i*-C_4H_8 submodel, including $H + O_2 \rightleftharpoons O + OH$ and $CH_3 + HO_2 \rightleftharpoons CH_3O + OH$.

3.3. Generalized NN-RS

The generalized NN architecture that considers both rate parameters and thermodynamic conditions has been illustrated in Fig. 3. Here we illustrate the utility of this NN architecture again using several examples. In the first example, we demonstrate an NN-RS for the laminar flame speed of methanol-air mixtures,

$$y_{S_u^\circ} = y_{S_u^\circ}(\mathbf{x}, T_0, p, \phi), \tag{17}$$

where T_0 is the unburned gas temperature (298 K $\le T_0 \le$ 450 K), p is the pressure ($0.5 \le p \le 10$ bar), and ϕ is the equivalence ratio ($0.6 \le \phi \le 1.8$). Here, $\mathbf{x} = [x_1, \ldots, x_K]^T$, where $K = 1052$, as discussed before. 60,000 total samples were created using Sobol sequences, by jointly perturbing the rate parameters $\mathbf{x}$ and the thermodynamic conditions T, p and ϕ. Fig. 10 show several projections of the generalized NN-RS in four dimensions, showing the variation of the laminar flame speed as a function of ϕ and the rate coefficient of $CH_3OH + OH \rightleftharpoons CH_3O + H_2O$. Each panel corresponds to a two-standard deviation value of the rates ($x = \pm 1$) for $H + O_2 \rightleftharpoons O + OH$ or $CO + OH \rightleftharpoons CO_2 + H$, all evaluated for $T_0 = 298$ K and $p = 1$ atm. Also shown on the $S_u^\circ - \phi$ planes are the experimental data reported under the same T_0 and p condi-

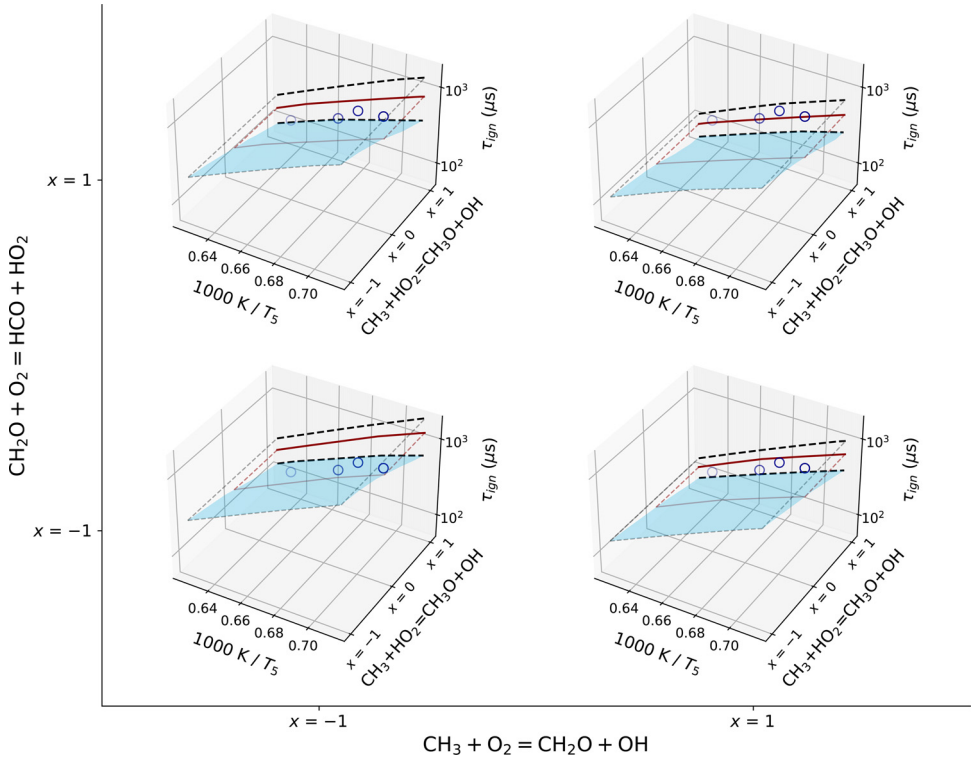

Fig. 11. Generalized NN-RS for ignition delay times of CH_4-O_2 mixtures diluted in X_{CO_2} = 75% - 95% for initial temperature $T_5 = 1250 - 1750$ K, pressure $p_5 = 1 - 100$ atm, equivalence ratio $\phi = 0.5 - 2.0$. Demonstrated here are ignition delay of a 3.91% CH_4-9.92%O_2-CO_2 mixture at $p_5 = 31.5$ atm. Symbols are experimental data [72]. The *x*- and *y*-axes vary the *A*-factors of reactions $CH_3 + O2 \rightleftharpoons CH_2O + OH$ and $CH_2O + O_2 \rightleftharpoons HCO + HO_2$, respectively. In each panel, NN-RS predictions were projected to illustrate the prediction uncertainty caused by the rate uncertainty of the reaction $CH_3 + HO_2 \rightleftharpoons CH_3O + OH$ of the trial FFCM-2 reaction model.

tions, over a range of equivalence ratios. On the same planes, we project three S_{ul}° profiles evaluated from the generalized NN-RS using the nominal rate value $x = 0$ for $CH_3OH + OH \rightleftharpoons CH_3O + H_2O$ (solid lines), and using $x = \pm 1$ of the same reaction (dashed lines). It can be seen that such plots and hence the underlying NN-RS are useful to quantifying the impact of rate parameters of a reaction model on the combustion property this model attempts to predict.

Further, we considered ignition delay times of $CH_4 - O_2$ mixtures diluted in X_{CO_2} = 75% - 95% for initial temperatures $T_5 =$ 1250 K to 1750 K, pressures $p_5 = 1$ atm to 100 atm and equivalence ratios $\phi = 0.5$ to 2.0. We created 200,000 uniform Sobol samples jointly for the rate parameters $\mathbf{x}$ ($K = 1052$) and the thermodynamic conditions T, p, X_{CO_2} and ϕ within the range specified. For $\mathbf{x}$, the uniform Sobol samples were converted to truncated normal distributions as discussed in previous section. Under all conditions, the generalized NN-RS was found to perform as well as those trained under each thermodynamic condition. Each panel in Fig. 11 shows the τ_{ign} projections of the generalized NN-RS in $1/T_5$ and the rate of $CH_3 + HO_2 \rightleftharpoons CH_3O + OH$, evaluated for a 3.91% CH_4-9.92% $O_2 - CO_2$ mixture at $p_5 = 31.5$ atm at four extreme rates of $x = \pm 1$ for reactions $CH_2O + O_2 \rightleftharpoons HCO + HO_2$ and $CH_3 + O_2 \rightleftharpoons CH_2O + OH$. Again shown in the τ_{ign} versus $1/T_5$ planes are the corresponding experimental data, and the model predictions for $x = 0$ (solid lines) and $x = \pm 1$ (dashed lines) of $CH_3 + HO_2 \rightleftharpoons CH_3O + OH$.

Another way to assess the accuracy of the generalized NN-RS is by comparing the ignition delays plotted using the Lifshitz correlation fitting by

$$\tau_{ign} = AT^n \exp\left(\frac{B}{T}\right)[CH_4]^{\alpha}[O_2]^{\beta}[CO_2]^{\gamma}. \quad (18)$$

Fig. 12 compares the correlation of Lifshitz correlation fitting using computer experiments using the unoptimized FFCM-2 on 10,000 samples of thermodynamic conditions for CH_4-O_2 mixtures diluted in $X_{CO_2} = 75\% - 95\%$ with initial temperature $T_5 = 1250$ K to 1750 K, pressure $p_5 = 1$ atm to 100 atm and equivalence ratios $\phi = 0.5$ to 2.0. We carried out regression analyses and obtained the 6 coefficients A, n, B, α, β, γ of Eq. (18) from these 10,000 samples, varying the rate coefficient of reaction R123 (CH_3+HO_2 $\rightleftharpoons$ CH_3O+OH) from its nominal value of $x = 0$ to the 2σ values of $x = 1$ and $x = -1$. The results are shown as solid lines in Fig. 12, where the error bars indicate the 2σ standard deviation of the fit. Using the generalized NN-RS, we also plot its predictions for the same 10,000 samples as symbols and the shaded bands, which indicates the 2σ band of the symbols. Clearly, the results shown indicate that the NN-RS is accurate in both the nominal values and their uncertainties over the broad range of thermodynamic and mixture conditions tested.

The pros and cons of the NN-RS under single thermodynamic condition and under more generalized thermodynamic conditions are quite obvious. When multiple thermodynamic conditions are selected as optimization targets, the use of a generalized NN-RS can reduce the total number of training samples significantly. However, a generalized NN-RS is deeper and has more parameters; it requires more training efforts, and more hyper-parameter tuning. In contrast, a simple NN-RS under one thermodynamic condition is smaller in its parameter size; requires a fewer number of training samples. As a result, the training process is easier to automate, as minimal hyper-parameter tuning is needed. In practice, simple NN-RSs are preferred when there are only few optimization targets to considered, and when the conditions are lightly correlated; the generalized NN-RS is more desirable for large-scale optimization with heavily correlated target conditions.

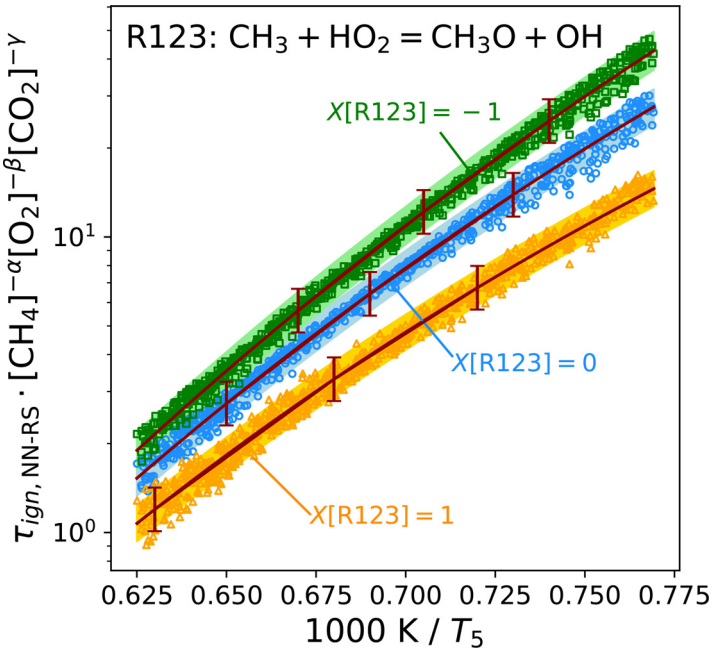

Fig. 12. Lifshitz correlations of the ignition delay time for CH_4-O_2 mixtures diluted in $X_{CO_2} = 75\% - 95\%$ for initial temperature $T_5 = 1250$ K to 1750 K, pressure $p_5 = 1$ atm to 100 atm and equivalence ratios $\phi = 0.5$ to 2.0. The solid lines are from regression of computer experiments using the trial FFCM-2 reaction model predictions varying the normalized rate coefficient of reaction R123 ($CH_3 + HO_2 \rightleftharpoons CH_3O + OH$) from its nominal value of $x = 0$ to the 2σ values of $x = 1$ and $x = -1$. The error bars indicate the 95% confidence interval (2σ standard deviation) of the regression fits. Symbols and shaded bands are calculated from the generalized NN-RS under respective conditions.

3.4. Optimization case study: FFCM-1a

In this section, we demonstrate the NN-MUM-PCE approach with a case study that optimizes the trial FFCM-2 and minimizes the model uncertainty using only the target set of FFCM-1 (a subset of FFCM-2). The 146 FFCM-1 targets covered the laminar flame speed, ignition delay time, and selected speciation data in shock tubes and flow reactors for H_2, syngas, CH_2O and CH_4 [26]. The resulting optimized model is termed FFCM-1a. With everything else being kept equal, the FFCM-1a optimization differs in two aspects from that of FFCM-1. For each optimization target, the truncated 20-parameter 2^{nd}-order polynomial response surface in FFCM-1 was replaced with an NN-RS that allows all parameters to vary. The sample size was 10,000 for laminar flame speeds and 40,000 for the ignition delay and species concentrations. We trained each NN-RS separately. The adaptive training technique and the generalized NN-RS architecture were not used in the current case study. Also differing from the FFCM-1 optimization was that the current optimization uses a trust region reflective (TRF) algorithm as opposed to the Levenberg-Marquardt algorithm used earlier [26]. For this specific case, the computational cost is discussed in Section S5 of the Supplementary Material (SM). Because FFCM-2 considers reactant fuels up to the size of C_4 and the FFCM-1 targets include C_{0-1} fuels only, many rate parameters and their uncertainties in FFCM-2 cannot be constrained by the FFCM-1 target set. And as expected, we found in an initial optimization run that many rate parameters see noise-level perturbations, and their 2σ uncertainty factor remain to be large. Hence, two threshold values were defined: the rate perturbation multiplier threshold χ_x and the rate 2σ uncertainty perturbation threshold $\chi_{2\sigma}$. If after optimization a rate parameter has multiplier close to unity $|A_k/A_{k,0} - 1| < \chi_x$ and its 2σ uncertainty remains to be larger than $\chi_{2\sigma}$, the rate parameter is deemed inactive and hence frozen. In this way, the rate parameters that cannot be constrained by the target set return to their nominal values, as discussed in Eq. (15) and Eq. (16).

Appropriate threshold values were studied in a parametric study. An example is shown in Fig. 13 for a fixed value of $\chi_{2\sigma} = 0.96$. As expected, an increase in χ_x leads to an initial rapid decrease in the number of active parameters that needs to be considered but the value of the cost function (e.g., the first term of Eq. (8)) increases only marginally. The parametric study suggests that $\chi_A = 0.05$ is appropriate because the cost function value increases by 3.5% but the number of active parameters dropped by 93%, from 1052 to 72. These threshold values were used in FFCM-1a optimization.

Summary results of the trial and optimized models are shown in several 45° diagonal plots of Fig. 14, comparing the performances of the reaction models before and after optimization against the target data values, and between the current FFCM-1a (the left two columns) and the original FFCM-1 (the right two columns). Three types of target data are plotted: the laminar flame speeds (top panels), shock tube ignition delays (middle panels), and species related targets (bottom panels). As it can be seen, the optimized FFCM-1a show improved predictions against the target experimental data, and in general, the maximum and RMS errors are reduced from the unoptimized FFCM-2 trial model to the optimized FFCM-1a model. Of equal importance is the model prediction uncertainties, calculated using Eq. (12), are reduced significantly, as demonstrated by the reduced error bar sizes of the model predictions. Comparing the plots in the second and fourth columns of Fig. 14, we also found that the performance of FFCM-1a is nearly identical to that of FFCM-1.

To further illustrate the effectiveness of the current NN-MUM-PCE approach, we plot in Fig. 15 three sample model validation sets, from the laminar flame speed of methane-air mixtures at 1 atm pressure and 298 K over a range of equivalence ratio (left column), the ignition delay of a 4.5% CH_4-19.1% O_2-Ar mixture at 1.96 atm (middle column), and the CH_3 time history profile of methane oxidation (0.2% CH_4-0.1% O_2-Ar at 1.02 atm and 2264 K) (right column). From the unoptimized FFCM-2 (top panels) to the optimized FFCM-1a (bottom panels), we see that a) the nominal predictions of the optimized model are improved notably for the ignition and CH_3 species profile targets, and b) as importantly, the prediction uncertainties of the optimized FFCM-

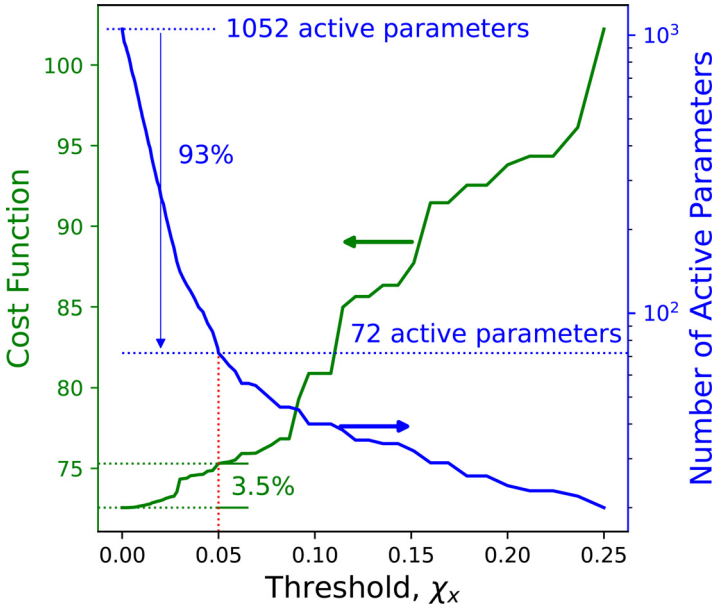

Fig. 13. Parametric study of the cost function (the first term of Eq. (8)) and the number of active parameters as a function of the rate threshold χ_x for FFCM-1a optimization. The uncertainty threshold $\chi_{2\sigma}$ value is fixed at 0.96.

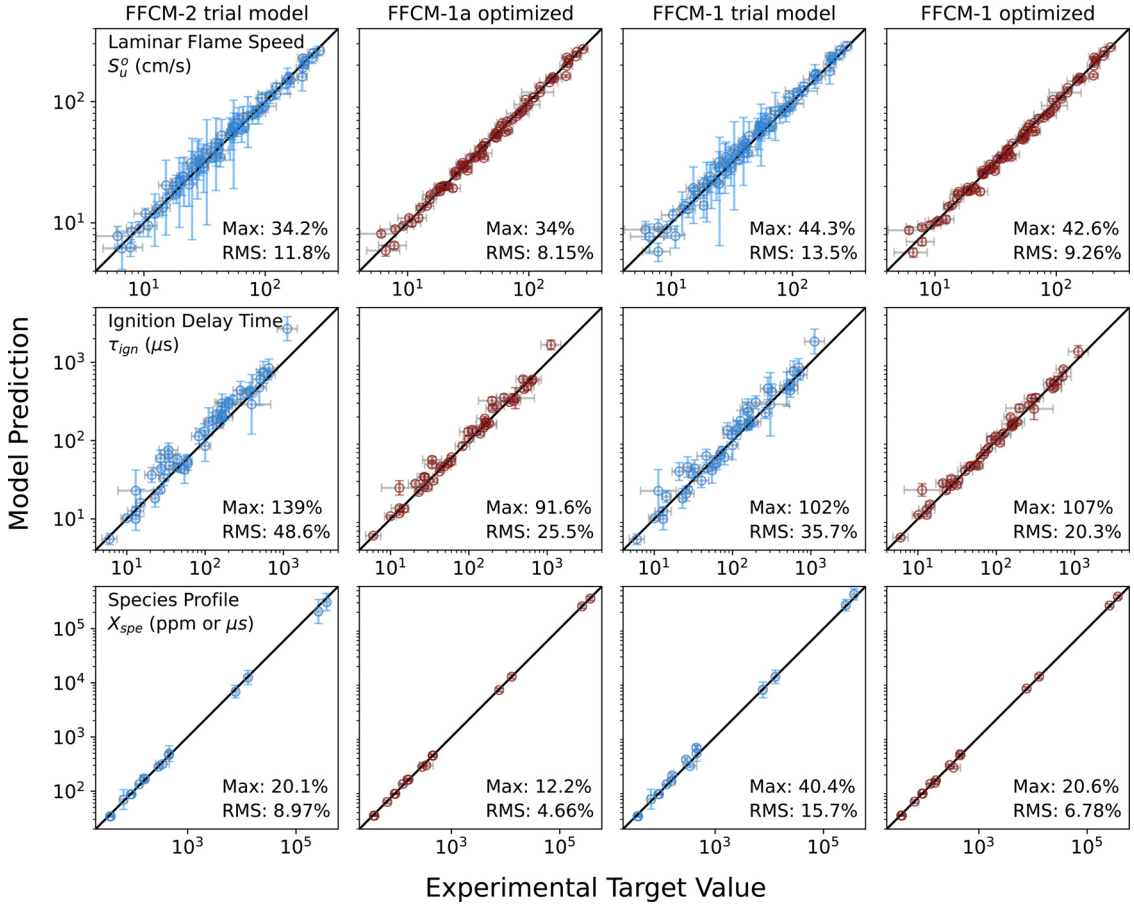

Fig. 14. Trial and optimized model predictions and their 2σ uncertainties for the laminar flame speed (top panels), shock tube ignition delay (middle panels) and selected species concentration (bottom panels) compared to experimental data and their 2σ uncertainty. Left two columns: FFCM-1a; right two columns: FFCM-1 [26]. In each panel the maximum and RMS errors of the model and experiment are indicated.

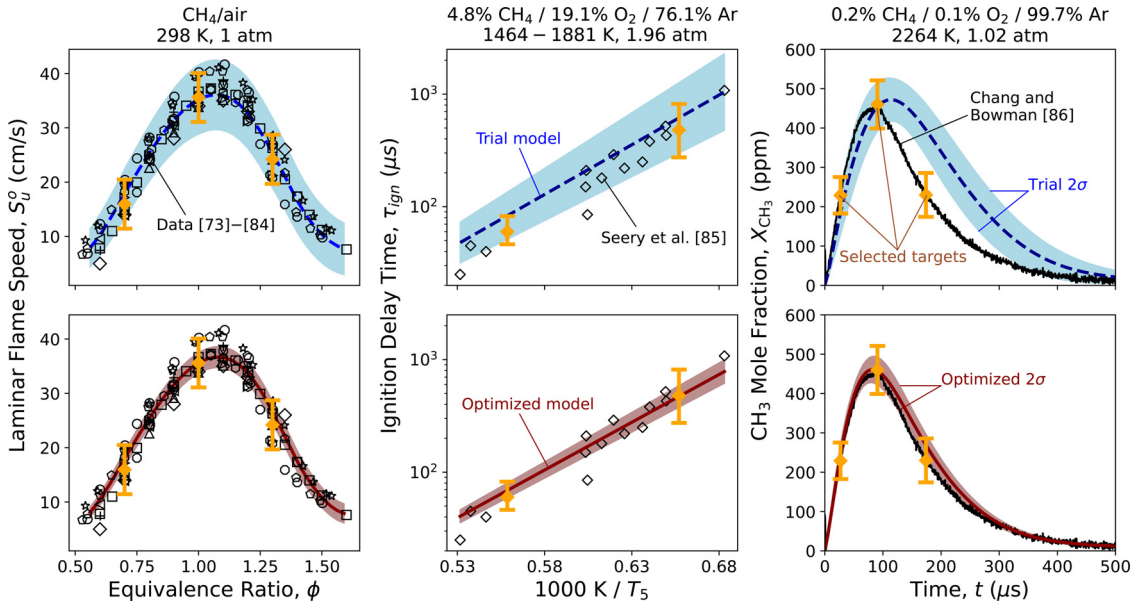

Fig. 15. Model predictions of unoptimized FFCM-2 (top panels) and optimized FFCM-1a (bottom panels) and respective experimental data (symbols). Left panels: laminar flame speed of methane-air at 1 atm and 298 K (symbols: ◇ Aung et al. [73]; □ Bosschaart and de Goey [74]; ○ Egolfopoulos et al. [75]; ◁ Hassan et al. [76]; ▷ Halter et al. [77]; ▽ Kobayashi et al. [78]; △ Lowry et al. [79]; ⬡ Park et al. [80]; + Rozenchan et al. [81]; ◯ Vagelopoulos and Egolfopoulos [82]; ☆ Yu et al. [83]; ⬠ Zhu et al. [84]); middle panels: ignition delay time of a 4.5% CH_4-19.1% O_2-Ar mixture at 1.96 atm (experimental data taken from ([85]); right panels: species time-history of CH_3 during shock tube oxidation of methane (0.2% CH_4-0.1% O_2-Ar) at 1.02 atm and 2264 K (experimental data taken from [86]). The dashed lines and shaded areas in the top panels are the trial model predictions and their 2σ uncertainty band; the solid lines and shade areas in the bottom panels are the corresponding results of the optimized FFCM-1a. The symbols marked by the error bars are the experimental targets and their 2σ uncertainties; they are parts of the FFCM-1 target set.

1a are reduced significantly for each of the targets shown in Fig. 15.

4. Conclusions

In this work, we explored the neural network approach to constructing response surfaces for reaction model optimization and uncertainty minimization. The study was motivated by the recent FFCM-2 effort. Compared to the earlier FFCM-1 effort, the parameter dimensionality and the target set size of FFCM-2 are significantly larger. As a result, the earlier response surface approach using 2^{nd}-order polynomials shows poor accuracy, efficiency and scalability. Key observations and conclusions are summarized below:

1. For large reaction model optimization, the polynomial response surface approach gives poor accuracy because of the need to define a set of active rate parameters, leading to significant truncation error.
2. In comparison, the neural network approach is found to be significantly more accurate, scalable and efficient than the polynomial response approach. The NN approach removes the need to define active parameters, thus eliminating the truncation errors; a shallow NN with only one hidden layer can handle over 1000 rate parameters as input variables, and a deep neural network enables the development of generalized NN response surfaces that consider both the rate parameters and thermodynamic and mixture conditions as the input variables.
3. We examined a various of NN features and explored optimal NN architectures for the response surface problems of relevance to reaction model optimization and uncertainty minimization, and demonstrated how adaptive NN training can improve the training efficiency.
4. We showed how the NN can be incorporated into the Method of Uncertainty Minimization using Polynomial Chaos Expansions (MUM-PCE), and demonstrated the resulting NN-MUM-PCE approach to the optimization of FFCM-1a, using FFCM-2 as the base trial reaction model and the FFCM-1 target set for optimization and uncertainty minimization.

The analyses and results discussed herein suggest that the neural network approach is robust and particularly suited for the optimization and uncertainty minimization of large reaction models.

Declaration of Competing Interest

The authors declare that they have no known competing financial interests or personal relationships that could have appeared to influence the work reported in this paper.

Acknowledgment

We acknowledge support through the Office of Naval Research (ONR) Grant No. N00014-21-1-2475 with Dr. Eric Marineau as Program Manager, and the Air Force Office of Scientific Research under Grant FA9550-16-1-0486 with Dr. Chiping Li as Program Manager.

Supplementary material

Supplementary material associated with this article can be found, in the online version, at doi:10.1016/j.combustflame.2023.112679

References

[1] H. Wang, D.A. Sheen, Combustion kinetic model uncertainty quantification, propagation and minimization, Prog. Energy Combust. Sci. 47 (2015) 1–31.
[2] D.A. Sheen, H. Wang, The method of uncertainty quantification and minimization using polynomial chaos expansions, Combust. Flame 158 (2011) 2358–2374.
[3] H. Wang, Chapter 14 - Uncertainty Quantification and Minimization, in: T. Faravelli, F. Manenti, E. Ranzi (Eds.), Mathematical Modelling of Gas-Phase Complex Reaction Systems: Pyrolysis and Combustion, Computer Aided Chemical Engineering, volume 45, Elsevier (2019), pp. 723–762.
[4] G.P. Smith, D.M. Golden, M. Frenklach, N.W. Moriarty, B. Eiteneer, M. Goldenberg, C.T. Bowman, R.K. Hanson, S. Song, W.C. Gardiner Jr, GRI-Mech (1999). http://www.me.berkeley.edu/gri_mech.

[5] M. Frenklach, H. Wang, M. Goldenberg, G. Smith, D. Golden, C. Bowman, R. Hanson, W. Gardiner, V. Lissianski, GRI-Mech-an optimized detailed chemical reaction mechanism for methane combustion, Gas Research Institute Topical Report No. GRI-95/0058 (1995).

[6] D.A. Sheen, X. You, H. Wang, T. Lovås, Spectral uncertainty quantification, propagation and optimization of a detailed kinetic model for ethylene combustion, Proc. Combust. Inst. 32 (2009) 535–542.

[7] M. Frenklach, H. Wang, M.J. Rabinowitz, Optimization and analysis of large chemical kinetic mechanisms using the solution mapping method-combustion of methane, Prog. Energy Combust. Sci. 18 (1992) 47–73.

[8] T. Varga, T. Nagy, C. Olm, I.G. Zsély, R. Pálvölgyi, E. Valkó, G. Vincze, M. Cserháti, H.J. Curran, T. Turányi, Optimization of a hydrogen combustion mechanism using both direct and indirect measurements, Proc. Combust. Inst. 35 (2015) 589–596.

[9] T. Nagy, E. Valkó, I. Sedyó, I.G. Zsély, M.J. Pilling, T. Turányi, Uncertainty of the rate parameters of several important elementary reactions of the H_2 and syngas combustion systems, Combust. Flame 162 (2015) 2059–2076.

[10] S.G. Davis, A.B. Mhadeshwar, D.G. Vlachos, H. Wang, A new approach to response surface development for detailed gas-phase and surface reaction kinetic model optimization, Int. J. Chem. Kinet. 36 (2003) 94–106.

[11] A.S. Tomlin, T. Ziehn, The use of global sensitivity methods for the analysis, evaluation and improvement of complex modelling systems, in: A.N. Gorban, D. Roose (Eds.), Coping with Complexity: Model Reduction and Data Analysis, Lecture Notes in Computational Science and Engineering, Springer, Berlin, Heidelberg (2011), pp. 9–36.

[12] T. Ziehn, A.S. Tomlin, GUI-HDMR - A software tool for global sensitivity analysis of complex models, Environ. Modell. Softw. 24 (2009) 775–785.

[13] M.S. Eldred, K.R. Dalbey, W.J. Bohnhoff, B.M. Adams, L.P. Swiler, P.D. Hough, D.M. Gay, J.P. Eddy, K.H. Haskell, DAKOTA : a multilevel parallel object-oriented framework for design optimization, parameter estimation, uncertainty quantification, and sensitivity analysis. Version 5.0, user's manual, Technical Report, 2010, doi:10.2172/991842.

[14] Y. Tao, H. Wang, Joint probability distribution of Arrhenius parameters in reaction model optimization and uncertainty minimization, Proc. Combust. Inst. 37 (2019) 817–824.

[15] D.A. Sheen, H. Wang, Combustion kinetic modeling using multispecies time histories in shock-tube oxidation of heptane, Combust. Flame 158 (2011) 645–656.

[16] S. Banerjee, R. Tangko, D.A. Sheen, H. Wang, C.T. Bowman, An experimental and kinetic modeling study of n-dodecane pyrolysis and oxidation, Combust. Flame 163 (2016) 12–30.

[17] O. Park, P.S. Veloo, D.A. Sheen, Y. Tao, F.N. Egolfopoulos, H. Wang, Chemical kinetic model uncertainty minimization through laminar flame speed measurements, Combust. Flame 172 (2016) 136–152.

[18] D.A. Sheen, J.A. Manion, Kinetics of the reactions of h and CH_3 radicals with n-butane: an experimental design study using reaction network analysis, J. Phys. Chem. A 118 (2014) 4929–4941.

[19] L. Cai, H. Pitsch, Optimized chemical mechanism for combustion of gasoline surrogate fuels, Combust. Flame 162 (2015) 1623–1637.

[20] L. Cai, H. Pitsch, Mechanism optimization based on reaction rate rules, Combust. Flame 161 (2014) 405–415.

[21] L. Cai, H. Pitsch, S.Y. Mohamed, V. Raman, J. Bugler, H. Curran, S.M. Sarathy, Optimized reaction mechanism rate rules for ignition of normal alkanes, Combust. Flame 173 (2016) 468–482.

[22] F. vom Lehn, L. Cai, H. Pitsch, Sensitivity analysis, uncertainty quantification, and optimization for thermochemical properties in chemical kinetic combustion models, Proc. Combust. Inst. 37 (2019) 771–779.

[23] L.A. Mertens, J.A. Manion, Kinetics of isopropanol decomposition and reaction with H atoms from shock tube experiments and rate constant optimization using the method of uncertainty minimization using polynomial chaos expansions (MUM-PCE), Int. J. Chem. Kinet. 53 (2021) 95–126.

[24] M. Fürst, A. Bertolino, A. Cuoci, T. Faravelli, A. Frassoldati, A. Parente, OptiSMOKE++: a toolbox for optimization of chemical kinetic mechanisms, Comput. Phys. Commun. 264 (2021) 107940.

[25] Y. Tao, G.P. Smith, H. Wang, Critical kinetic uncertainties in modeling hydrogen/carbon monoxide, methane, methanol, formaldehyde, and ethylene combustion, Combust. Flame 195 (2018) 18–29.

[26] G. Smith, Y. Tao, H. Wang, Foundational Fuel Chemistry Model Version 1.0 (FFCM-1), https://www.web.stanford.edu/group/haiwanglab/FFCM1/pages/FFCM1.html(2017).

[27] H. Wang, R. Xu, K. Wang, C.T. Bowman, R.K. Hanson, D.F. Davidson, K. Brezinsky, F.N. Egolfopoulos, A physics-based approach to modeling real-fuel combustion chemistry - I. Evidence from experiments, and thermodynamic, chemical kinetic and statistical considerations, Combust. Flame 193 (2018) 502–519.

[28] R. Xu, K. Wang, S. Banerjee, J. Shao, T. Parise, Y. Zhu, S. Wang, A. Movaghar, D.J. Lee, R. Zhao, X. Han, Y. Gao, T. Lu, K. Brezinsky, F.N. Egolfopoulos, D.F. Davidson, R.K. Hanson, C.T. Bowman, H. Wang, A physics-based approach to modeling real-fuel combustion chemistry - II. Reaction kinetic models of jet and rocket fuels, Combust. Flame 193 (2018) 520–537.

[29] Y. Tao, R. Xu, K. Wang, J. Shao, S.E. Johnson, A. Movaghar, X. Han, J.-W. Park, T. Lu, K. Brezinsky, F.N. Egolfopoulos, D.F. Davidson, R.K. Hanson, C.T. Bowman, H. Wang, A physics-based approach to modeling real-fuel combustion chemistry - III. Reaction kinetic model of JP10, Combust. Flame 198 (2018) 466–476.

[30] K. Wang, R. Xu, T. Parise, J. Shao, A. Movaghar, D.J. Lee, J.-W. Park, Y. Gao, T. Lu, F.N. Egolfopoulos, D.F. Davidson, R.K. Hanson, C.T. Bowman, H. Wang, A physics-based approach to modeling real-fuel combustion chemistry - IV. HyChem modeling of combustion kinetics of a bio-derived jet fuel and its blends with a conventional jet A, Combust. Flame 198 (2018) 477–489.

[31] C. Saggese, K. Wan, R. Xu, Y. Tao, C.T. Bowman, J.-W. Park, T. Lu, H. Wang, A physics-based approach to modeling real-fuel combustion chemistry - V. NOx formation from a typical Jet A, Combust. Flame 212 (2020) 270–278.

[32] R. Xu, C. Saggese, R. Lawson, A. Movaghar, T. Parise, J. Shao, R. Choudhary, J.-W. Park, T. Lu, R.K. Hanson, D.F. Davidson, F.N. Egolfopoulos, A. Aradi, A. Prakash, V.R.R. Mohan, R. Cracknell, H. Wang, A physics-based approach to modeling real-fuel combustion chemistry - VI. Predictive kinetic models of gasoline fuels, Combust. Flame 220 (2020) 475–487.

[33] R. Xu, H. Wang, A physics-based approach to modeling real-fuel combustion chemistry - VII. Relationship between speciation measurement and reaction model accuracy, Combust. Flame 224 (2021) 126–135.

[34] Y. Zhang, W. Dong, L. Vandewalle, R. Xu, G. Smith, H. Wang, Foundational Fuel Chemistry Model Version 2.0 (FFCM-2), https://www.web.stanford.edu/group/haiwanglab/FFCM2/pages/FFCM2.html(2022).

[35] A. Krizhevsky, I. Sutskever, G.E. Hinton, ImageNet classification with deep convolutional neural networks, Advances in Neural Information Processing Systems, volume 25, 2012.

[36] P. Sun, H. Kretzschmar, X. Dotiwalla, A. Chouard, V. Patnaik, P. Tsui, J. Guo, Y. Zhou, Y. Chai, B. Caine, V. Vasudevan, W. Han, J. Ngiam, H. Zhao, A. Timofeev, S. Ettinger, M. Krivokon, A. Gao, A. Joshi, Y. Zhang, J. Shlens, Z. Chen, D. Anguelov, Scalability in perception for autonomous driving: Waymo open dataset, 2020 IEEE/CVF Conference on Computer Vision and Pattern Recognition (CVPR), IEEE, Seattle, WA, USA (2020), pp. 2443–2451.

[37] S.D. Holcomb, W.K. Porter, S.V. Ault, G. Mao, J. Wang, Overview on DeepMind and its AlphaGo Zero AI, Proceedings of the 2018 International Conference on Big Data and Education, ICBDE '18, Association for Computing Machinery, New York, NY, USA (2018), pp. 67–71.

[38] J. Devlin, M.-W. Chang, K. Lee, K. Toutanova, BERT: Pre-training of deep bidirectional transformers for language understanding, 2019, 10.48550/arXiv.1810.04805

[39] J. Howard, S. Ruder, Universal language model fine-tuning for text classification, 2018, 10.48550/arXiv.1801.06146

[40] M. Ihme, W.T. Chung, A.A. Mishra, Combustion machine learning: principles, progress and prospects, Prog. Energy Combust. Sci. 91 (2022) 101010.

[41] L. Zhou, Y. Song, W. Ji, H. Wei, Machine learning for combustion, Energy AI 7 (2022) 100128.

[42] Y. Wang, W. Wei, Y. Zhang, R.K. Hanson, A new strategy of characterizing hydrocarbon fuels using ftir spectra and generalized linear model with grouped-lasso regularization, Fuel 287 (2021) 119419.

[43] W. Ji, W. Qiu, Z. Shi, S. Pan, S. Deng, Stiff-PINN: physics-informed neural network for stiff chemical kinetics, J. Phys. Chem. A 125 (2021) 8098–8106.

[44] T. Zhang, Y. Yi, Y. Xu, Z.X. Chen, Y. Zhang, W. E, Z.-Q.J. Xu, A multi-scale sampling method for accurate and robust deep neural network to predict combustion chemical kinetics, Combust. Flame 245 (2022) 112319.

[45] W. Ji, S. Deng, Autonomous discovery of unknown reaction pathways from data by chemical reaction neural network, J. Phys. Chem. A 125 (2021) 1082–1092.

[46] B. Yang, Towards predictive combustion kinetic models: progress in model analysis and informative experiments, Proc. Combust. Inst. 38 (2021) 199–222.

[47] S. Li, B. Yang, F. Qi, Accelerate global sensitivity analysis using artificial neural network algorithm: case studies for combustion kinetic model, Combust. Flame 168 (2016) 53–64.

[48] J. Wang, Z. Zhou, K. Lin, C.K. Law, B. Yang, Facilitating Bayesian analysis of combustion kinetic models with artificial neural network, Combust. Flame 213 (2020) 87–97.

[49] A. Paszke, S. Gross, F. Massa, A. Lerer, J. Bradbury, G. Chanan, T. Killeen, Z. Lin, N. Gimelshein, L. Antiga, et al., PyTorch: an imperative style, high-performance deep learning library, Adv. Neural Inf. Process. Syst. 32 (2019).

[50] D.G. Goodwin, R.L. Speth, H.K. Moffat, B.W. Weber, Cantera: An object-oriented software toolkit for chemical kinetics, thermodynamics, and transport processes(2021). https://www.cantera.org.

[51] A.F. Agarap, Deep learning using Rectified Linear Units (ReLU), 2019, 10.48550/arXiv.1803.08375

[52] I.M. Sobol', On the distribution of points in a cube and the approximate evaluation of integrals, Comput. Math. Math. Phys. 7 (1967) 86–112.

[53] E. Hébrard, A.S. Tomlin, R. Bounaceur, F. Battin-Leclerc, Determining predictive uncertainties and global sensitivities for large parameter systems: a case study for n-butane oxidation, Proc. Combust. Inst. 35 (2015) 607–616.

[54] T. Hastie, R. Tibshirani, J. Friedman, The elements of statistical learning, Springer Series in Statistics, Springer, New York, NY, 2009, doi:10.1007/978-0-387-84858-7.

[55] L.N. Smith, A disciplined approach to neural network hyper-parameters: Part 1 – learning rate, batch size, momentum, and weight decay, 2018, 10.48550/arXiv.1803.09820

[56] A. Lifshitz, K. Scheller, A. Burcat, G.B. Skinner, Shock-tube investigation of ignition in methane-oxygen-argon mixtures, Combust. Flame 16 (1971) 311–321.

[57] J.J. Moré, The Levenberg-Marquardt Algorithm: Implementation and Theory, Numerical analysis, Springer (1978), pp. 105–116.

[58] P. Virtanen, R. Gommers, T.E. Oliphant, M. Haberland, T. Reddy, D. Cournapeau, E. Burovski, P. Peterson, W. Weckesser, J. Bright, S.J. van der Walt, M. Brett, J. Wilson, K.J. Millman, N. Mayorov, A.R.J. Nelson, E. Jones, R. Kern, E. Larson, C.J. Carey, I. Polat, Y. Feng, E.W. Moore, J. VanderPlas, D. Laxalde, J. Perktold, R. Cimrman, I. Henriksen, E.A. Quintero, C.R. Harris, A.M. Archibald, A.H. Ribeiro, F. Pedregosa, P. van Mulbregt, SciPy 1.0 Contributors, A. Vijaykumar, A.P. Bardelli, A. Rothberg, A. Hilboll, A. Kloeckner, A. Scopatz, A. Lee,

A. Rokem, C.N. Woods, C. Fulton, C. Masson, C. Häggström, C. Fitzgerald, D.A. Nicholson, D.R. Hagen, D.V. Pasechnik, E. Olivetti, E. Martin, E. Wieser, F. Silva, F. Lenders, F. Wilhelm, G. Young, G.A. Price, G.-L. Ingold, G.E. Allen, G.R. Lee, H. Audren, I. Probst, J.P. Dietrich, J. Silterra, J.T. Webber, J. Slavič, J. Nothman, J. Buchner, J. Kulick, J.L. Schönberger, J.V. de Miranda Cardoso, J. Reimer, J. Harrington, J.L.C. Rodríguez, J. Nunez-Iglesias, J. Kuczynski, K. Tritz, M. Thoma, M. Newville, M. Kümmerer, M. Bolingbroke, M. Tartre, M. Pak, N.J. Smith, N. Nowaczyk, N. Shebanov, O. Pavlyk, P.A. Brodtkorb, P. Lee, R.T. McGibbon, R. Feldbauer, S. Lewis, S. Tygier, S. Sievert, S. Vigna, S. Peterson, S. More, T. Pudlik, T. Oshima, T.J. Pingel, T.P. Robitaille, T. Spura, T.R. Jones, T. Cera, T. Leslie, T. Zito, T. Krauss, U. Upadhyay, Y.O. Halchenko, Y. Vázquez-Baeza, SciPy 1.0: fundamental algorithms for scientific computing in Python, Nat. Methods 17 (2020) 261–272.

[59] S. Mei, A. Montanari, The generalization error of random features regression: precise asymptotics and the double descent curve, Comm. Pure Appl. Math. 75 (2022) 667–766.

[60] C.W. Zhou, J.M. Simmie, K.P. Somers, C.F. Goldsmith, H.J. Curran, Chemical kinetics of hydrogen atom abstraction from allylic sites by $^3O_2$; implications for combustion modeling and simulation, J. Phys. Chem. A 121 (2017) 1890–1899.

[61] T. Ingham, R. Walker, R. Woolford, Kinetic parameters for the initiation reaction $RH + O_2 = R + HO_2$, Symp. (Int.) Combust. 25 (1994) 767–774.

[62] M.E. Bardin, E.V. Ivanov, E.J. Nilsson, V.A. Vinokurov, A.A. Konnov, Laminar burning velocities of dimethyl carbonate with air, Energy Fuels 27 (2013) 5513–5517.

[63] S.G. Davis, C. Law, Determination of and fuel structure effects on laminar flame speeds of C_1 to C_8 hydrocarbons, Combust. Sci. Technol. 140 (1998) 427–449.

[64] F. Egolfopoulos, D. Du, C. Law, A study on ethanol oxidation kinetics in laminar premixed flames, flow reactors, and shock tubes, Symp. (Int.) Combust. 24 (1992) 833–841.

[65] Ö.L. Gülder, Laminar burning velocities of methanol, ethanol and isooctane-air mixtures, Symp. (Int.) Combust. 19 (1982) 275–281.

[66] A. Katoch, M. Asad, S. Minaev, S. Kumar, Measurement of laminar burning velocities of methanol-air mixtures at elevated temperatures, Fuel 182 (2016) 57–63.

[67] M. Metghalchi, J.C. Keck, Burning velocities of mixtures of air with methanol, isooctane, and indolene at high pressure and temperature, Combust. Flame 48 (1982) 191–210.

[68] L. Sileghem, V. Alekseev, J. Vancoillie, E. Nilsson, S. Verhelst, A. Konnov, Laminar burning velocities of primary reference fuels and simple alcohols, Fuel 115 (2014) 32–40.

[69] K. Saeed, C.R. Stone, Measurements of the laminar burning velocity for mixtures of methanol and air from a constant-volume vessel using a multizone model, Combust. Flame 139 (2004) 152–166.

[70] J. Vancoillie, M. Christensen, E.J. Nilsson, S. Verhelst, A.A. Konnov, Temperature dependence of the laminar burning velocity of methanol flames, Energy Fuels 26 (2012) 1557–1564.

[71] S. Voss, F. Rau, V.A. Alekseev, A.A. Konnov, R. Haas-WittmüSS, R.T.E. Hermanns, E. Volkov, L.P.H.D. Goey, A comparative study of laminar burning velocities of methane, methanol and ethanol using the heat flux method, Proceedings of the European Combustion Meeting (2015).

[72] J. Shao, R. Choudhary, D.F. Davidson, R.K. Hanson, S. Barak, S. Vasu, Ignition delay times of methane and hydrogen highly diluted in carbon dioxide at high pressures up to 300 atm, Proc. Combust. Inst. 37 (2019) 4555–4562.

[73] K. Aung, L.-K. Tseng, M. Ismail, G. Faeth, Response to comment by S.C. Taylor and D.B. Smith on "laminar burning velocities and Markstein numbers of hydrocarbon/air flames", Combust. Flame 102 (1995) 526–530.

[74] K. Bosschaart, L. de Goey, The laminar burning velocity of flames propagating in mixtures of hydrocarbons and air measured with the heat flux method, Combust. Flame 136 (2004) 261–269.

[75] F. Egolfopoulos, P. Cho, C. Law, Laminar flame speeds of methane-air mixtures under reduced and elevated pressures, Combust. Flame 76 (1989) 375–391.

[76] M. Hassan, K. Aung, G. Faeth, Measured and predicted properties of laminar premixed methane/air flames at various pressures, Combust. Flame 115 (1998) 539–550.

[77] F. Halter, T. Tahtouh, C. Mounaïm-Rousselle, Nonlinear effects of stretch on the flame front propagation, Combust. Flame 157 (2010) 1825–1832.

[78] H. Kobayashi, K. Seyama, H. Hagiwara, Y. Ogami, Burning velocity correlation of methane/air turbulent premixed flames at high pressure and high temperature, Proc. Combust. Inst. 30 (2005) 827–834.

[79] W. Lowry, J. de Vries, M. Krejci, E. Petersen, Z. Serinyel, W. Metcalfe, H. Curran, G. Bourque, Laminar flame speed measurements and modeling of pure alkanes and alkane blends at elevated pressures, J. Eng. Gas Turbines Power 133 (2011).

[80] O. Park, P.S. Veloo, N. Liu, F.N. Egolfopoulos, Combustion characteristics of alternative gaseous fuels, Proc. Combust. Inst. 33 (2011) 887–894.

[81] G. Rozenchan, D. Zhu, C. Law, S. Tse, Outward propagation, burning velocities, and chemical effects of methane flames up to 60 atm, Proc. Combust. Inst. 29 (2002) 1461–1470.

[82] C.M. Vagelopoulos, F.N. Egolfopoulos, Direct experimental determination of laminar flame speeds, Symp. (Int.) Combust. 27 (1998) 513–519.

[83] G. Yu, C. Law, C. Wu, Laminar flame speeds of hydrocarbon + air mixtures with hydrogen addition, Combust. Flame 63 (1986) 339–347.

[84] D. Zhu, F. Egolfopoulos, C. Law, Experimental and numerical determination of laminar flame speeds of methane/(Ar, N_2, CO_2)-air mixtures as function of stoichiometry, pressure, and flame temperature, Symp. (Int.) Combust. 22 (1989) 1537–1545.

[85] D.J. Seery, C.T. Bowman, An experimental and analytical study of methane oxidation behind shock waves, Combust. Flame 14 (1970) 37–47.

[86] A. Chang, D. Davidson, M. DiRosa, R. Hanson, C. Bowman, Shock tube experiments for development and validation of kinetic models of hydrocarbon oxidation, 25th Symp. (Int.) Combust., Poster (1994), pp. 3–23.